CHAPTER IV

Oxygen isotopic response to late Cenozoic Andean surface uplift

4.1 Abstract

The timing and magnitude of surface uplift provides important constraints on geodynamic models of orogen formation. Oxygen isotopes and Δ_{47} clumped isotopes from terrestrial sediments have been used with modern isotope and temperature lapse rates to infer past surface elevations of the Andes. However, these interpretations are contentious because variations in the oxygen isotope composition in meteoric water ($\delta^{18}O_p$) are caused by changes in both elevation (orographic) and regional climate. Here, we use a limited-domain isotope-tracking general circulation model to simulate changes in $\delta^{18}O_p$ and isotopic lapse rates in response to Andean surface uplift, and to re-evaluate $\delta^{18}O$ depletion and Δ_{47} clumped isotope changes in late Miocene carbonates previously interpreted to reflect rapid Andean growth. Results indicate that Andean surface uplift leads to changes in low-level atmospheric circulation and an increase in precipitation along the eastern Andean flank which influences isotopic source and amount effects. Simulated changes in Andean $\delta^{18}O_p$ are not systematic with an increase in surface elevation, but are instead a function of orographic thresh-

Official citation:
Insel, N., C.J. Poulsen, T.A. Ehlers, C. Sturm, (in review with coauthors). Oxygen isotopic response to late Cenozoic Andean surface uplift *EPSL*

old conditions that abruptly change regional climate. A $\delta^{18}O_p$ decrease of >5‰ over the central Andes and an increase in isotopic lapse rates (up to 0.8‰ km^{-1}) coincide with Andean surface uplift from 75 to 100% of modern elevation. These changes in the isotopic signature could account for the entire 3-4‰ $\delta^{18}O$ depletion in late Miocene carbonate nodules, and suggest an Andean paleoelevation of ∼3000 m (75% of modern elevations) before 10 Ma.

4.2 Introduction

The timing and rates at which current Andean Plateau (AP) elevations were attained are strongly debated. Recent elevation reconstructions of the AP suggest a rapid and recent rise of ∼2.5 ± 1 km of elevation (from paleoelevations ≤1000 m) of the central Andes during the late Miocene (10-6 Ma) in response to lithospheric delamination under the Bolivian AP (e.g., Garzione et al., 2008, 2006; Ghosh et al., 2006b). This result has recently been challenged by paleoclimate modeling studies that have highlighted the sensitivity of paleoaltimetry interpretations to climate change (Ehlers and Poulsen, 2009; Insel et al., 2009; Poulsen et al., 2010). Furthermore, geological and recent biotaxa evidence suggest AP growth was slow and steady since at least the Eocene (∼40 Ma), which implies elevations of ∼2000 m prior to 20-10 Ma (e.g., Alpers and Brimhall, 1988; Barnes and Ehlers, 2009; Picard et al., 2008; Rech et al., 2006; Schlunegger et al., 2010; Sebrier et al., 1988). Thus, significant debate exists on elevation history of the AP and the influence of climate change on paleo-elevation reconstructions.

Oxygen isotope paleoaltimetry is assumed to provide the most robust estimation of Andean paleoelevations. This approach uses preserved $\delta^{18}O$ in geological archives

(e.g. carbonates, silicates, volcanic glasses) as a proxy for ancient meteoric $\delta^{18}O$. The composition of $\delta^{18}O$ ($\delta^{18}O = ([(^{18}O/^{16}O)_{sample} / (^{18}O/^{16}O)_{standard}]\text{-}1)*1000$) in these archives is controlled by the temperature and the composition of meteoric water at the time of mineral formation, both of which are related to elevation (e.g., Chamberlain et al., 1999; Drummond et al., 1993; Siegenthaler and Oeschger, 1980). The elevation - $\delta^{18}O_p$ relationship reflects Rayleigh distillation of the heavy isotope (^{18}O) through condensation and precipitation as air masses are adiabatically cooled (e.g., Poage and Chamberlain, 2001). Rayleigh distillation is an exponential relationship that describes the partitioning of isotopes between two reservoirs as one reservoir decreases in size. Due to the correlation between $\delta^{18}O$ of meteoric water and elevation, mountain surface uplift can be reconstructed through stable isotope studies of authigenic (in-situ formed) minerals, assuming isotopic lapse rates (the rate of change in isotopic composition with altitude) are linear and similar to modern. Based on these assumptions, a 3-4‰ $\delta^{18}O$ shift in late Miocene carbonate nodules from the AP has been interpreted to reflect substantial surface uplift (Garzione et al., 2006; Ghosh et al., 2006b).

However, several factors other than elevation change influence the modern climatology of $\delta^{18}O_p$ along the Andes, such as precipitation (amount effect), water vapor source, and wind patterns (e.g., Insel et al., in review; Vuille et al., 2003). General atmospheric circulation models indicate that Andean surface uplift causes substantial changes in South American regional climate (e.g., Ehlers and Poulsen, 2009; Garreaud et al., 2010; Insel et al., 2009; Poulsen et al., 2010). In particular, an abrupt increase in Andean precipitation and convection is associated with Andean threshold elevations of 50-70% of modern heights (Insel et al., 2009; Poulsen et al., 2010). Simulated changes in regional paleoclimate can influence isotopic fractiona-

tion and source effects that cause dramatic changes in the paleo $\delta^{18}O_p$ composition (Ehlers and Poulsen, 2009). Thus, late Miocene changes in central Andean $\delta^{18}O$ could also be related to the intensification of precipitation associated with relatively minor surface uplift (Poulsen et al., 2010).

Previous paleoclimate modeling studies have indicated the potential impact of increasing convective precipitation on paleoaltimetry estimations, but are limited in their ability to provide direct regional estimations of $\delta^{18}O_p$ changes and isotopic lapse rates in response to elevation and climate change. Previous studies used either high-resolution non-isotope tracking regional models (e.g., Ehlers and Poulsen, 2009; Insel et al., 2009) or coarser resolution global scale models with isotope tracking capabilities (e.g., Poulsen et al., 2010) that have limitations in regions with steep topography imposed by spectral smoothing. In this study we complement previous work by using a high- resolution limited-domain general circulation model with isotope diagnostics (REMOiso). This approach provides a better representation of Andean topography at a horizontal resolution that approaches the spatial scales represented by proxy data. Results highlight the behavior of $\delta\ ^{18}O_p$ under past topographic and climate conditions and refines orographic threshold elevations for significant changes in $\delta\ ^{18}O_p$. Specifically, we (1) estimate changes in $\delta^{18}O\ _p$ due to Andean surface uplift and provide predictions of precipitation patterns and $\delta^{18}O_p$ for specific Andean heights; (2) quantify the changes in isotopic lapse rates in response to Andean surface uplift; and (3) evaluate the geological/isotopic evidence for surface uplift. The integration of model results and observations suggests that regional climate change in response to surface uplift caused changes in the stable isotope record.

4.3 Method

To quantify the influence of Andean surface uplift on $\delta^{18}O_p$ and oxygen isotopic lapse rates, we use a numerical three-dimensional limited-domain general circulation model with isotope-tracking capabilities (REMOiso) (Sturm et al., 2007a, 2005). Isotope fractionation and transport processes are embedded at all stages of the hydrological cycle by defining isotopic counterparts to all water-related variables. Therefore, the species H_2O^{18} and HDO are treated independently from the predominant H_2O^{16}, but undergo the same processes including equilibrium and kinetic fractionations (Sturm et al., 2005). Stable water isotopes are treated as passive tracers in soil moisture and snow layer and all vapor fluxes from the surface are considered non-fractionating. All experiments are forced using modern boundary conditions, including stable water isotopes, from the ECHAM-4 global climate model with specified SSTs derived from monthly satellite data (i.e. HadSST; Hoffmann et al. 1998).

Simulations were performed for South America using a continental-scale domain with 0.5° (∼55 km) horizontal resolution consisting of 160x120 grid points and 31 vertical levels (Fig. 4.1). Three experiments were completed with Andean elevations representing 100%, 75%, and 50% of the modern Andes height. In other regions of South America, the topography was maintained at modern elevations. All other parameters remain the same between experiments. All three experiments were integrated for 10 years with boundary conditions for the interval 1989 to 1998. Because of the high computational cost, it was not practical to run REMOiso continuously for 10 years. Instead, 15-month integrations consisting of the individual year and three prior months (October-December) were run. Each simulation year was initialized from a spin-up simulation of 21 months (January to September) with boundary

conditions for year 1993 to assure the same initial conditions for each simulation in the experiment series. Year 1993 was chosen for the spin-up, because it most closely resembled the 30-yr precipitation mean over the study area.

We present simulated annual amount-weighted mean $\delta^{18}O_p$ and isotopic lapse rates based on 10-year averages. Isotopic lapse rates are calculated every 0.55° latitude by linear regression of $\delta\ ^{18}O_p$ for all grid points between peak and flank (∼300 m) elevations. Absolute values of isotopic lapse rates are presented as the 4 point (2°) running average.

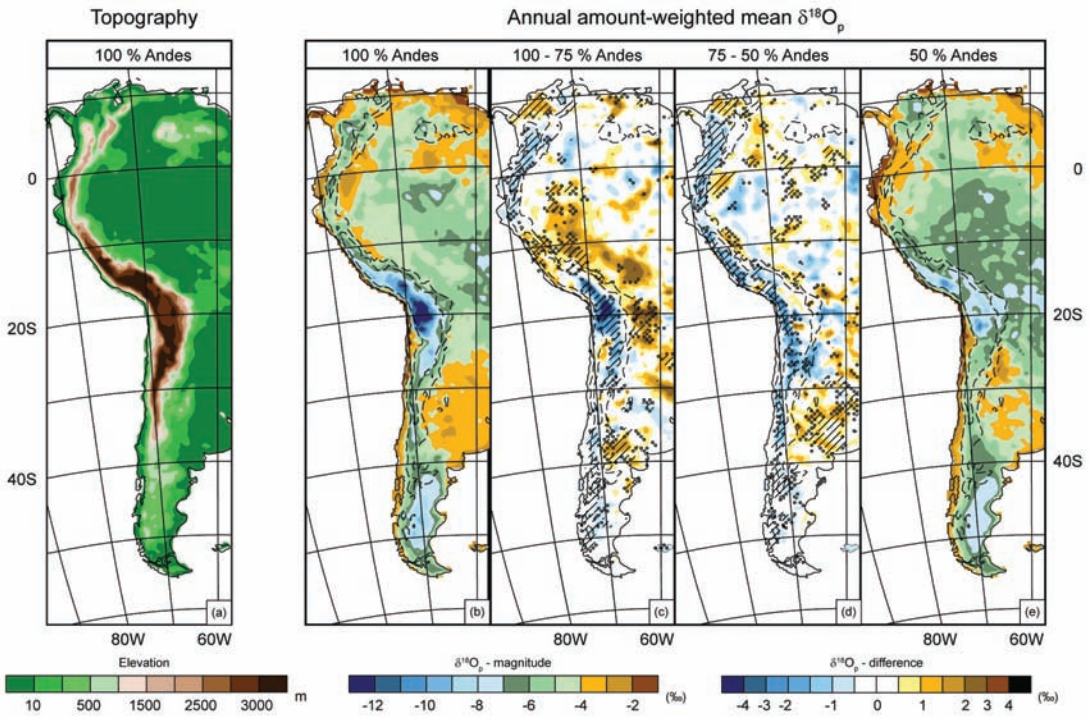

Figure 4.1: Topography and simulated annual amount-weighted mean $\delta^{18}\ O_p$ (‰) along the Andes. Dashed lines represent 1000 and 3000 m contour lines. (a) Present-day topography (m) used in the model for 100% Andes simulations. (b-e) Panel plots showing changes in $\delta^{18}O_p$ with increasing Andean elevations. (e) Absolute values of $\delta^{18}O_p$ for 50% Andean height simulations, (d) difference in $\delta^{18}O_p$ between 75 and 50% Andes, (c) difference in $\delta^{18}O_p$ between 100 and 75% Andes, and (b) absolute $\delta^{18}O_p$ compositions for simulations with 100% Andes, respectively. Stippled circle regions show areas where $\delta^{18}O_p$ changes are significant at the 80-90% confidence level, dashed pattern indicates regions where $\delta^{18}O_p$ changes are significant at the >90% confidence level.

4.4 Results

4.4.1 Modern isotope climatology

REMOiso has been shown to realistically simulate modern large-scale climate and circulation patterns, and spatial variations in $\delta^{18}O_p$ in South America (Insel et al., in review; Sturm et al., 2007a,b). In agreement with observations, simulated $\delta^{18}O_p$ is relatively high (-3 to -6 ‰) over the Amazon Basin due to evapotranspiration (Fig. 4.1b, 100% Andes). Once air masses reach the Andes, adiabatic cooling and condensation associated with rising air masses contribute to the isotopic depletion of vapor. Strong convergence, vertical ascent and rainout along the eastern Andean flank result in significant Rayleigh distillation which causes $\delta^{18}O_p$ to exponentially decrease with cumulative precipitation, and results in the lowest $\delta^{18}O_p$ ($<$ -12‰) at high elevation sites along the Andes (Fig. 4.1b). Low $\delta\ ^{18}O_p$ (-7 to -10‰) is also simulated in southern South America due to the latitudinal effect.

Simulated modern isotopic lapse rates vary significantly along the Andes (Fig. 4.2a and 4.2e). Along the eastern flank, modern lapse rates range from -2.09‰ km^{-1} to 1.02‰ km^{-1} between 10°N and 50°S (Fig. 4.2a). Along the western flank, simulated modern lapse rates vary between -3.46‰ km^{-1} and 0.22‰ km^{-1} (Fig. 4.2e). Overall, the largest lapse rates exist over the AP at ∼20°S and in the southern Andes south of ∼ 37°S. Lapse rates can be positive ($\delta^{18}O_p$ increases with altitude) where modern peak elevations in the model are below 2000 m (Fig. 4.2a, b, e, f). In the southern Andes, positive lapse rates along the eastern flank are mainly related to an isotopic rain shadow effect, where the steady eastward decrease in $\delta^{18}O_p$ reflects the increasing distance from the principal water vapor source (South Pacific) (Stern and Blisniuk, 2002) and spillover of condensate to the leeward (eastern) side leads to further depletion of $\delta^{18}O_p$ along the eastern flank with decreasing altitude.

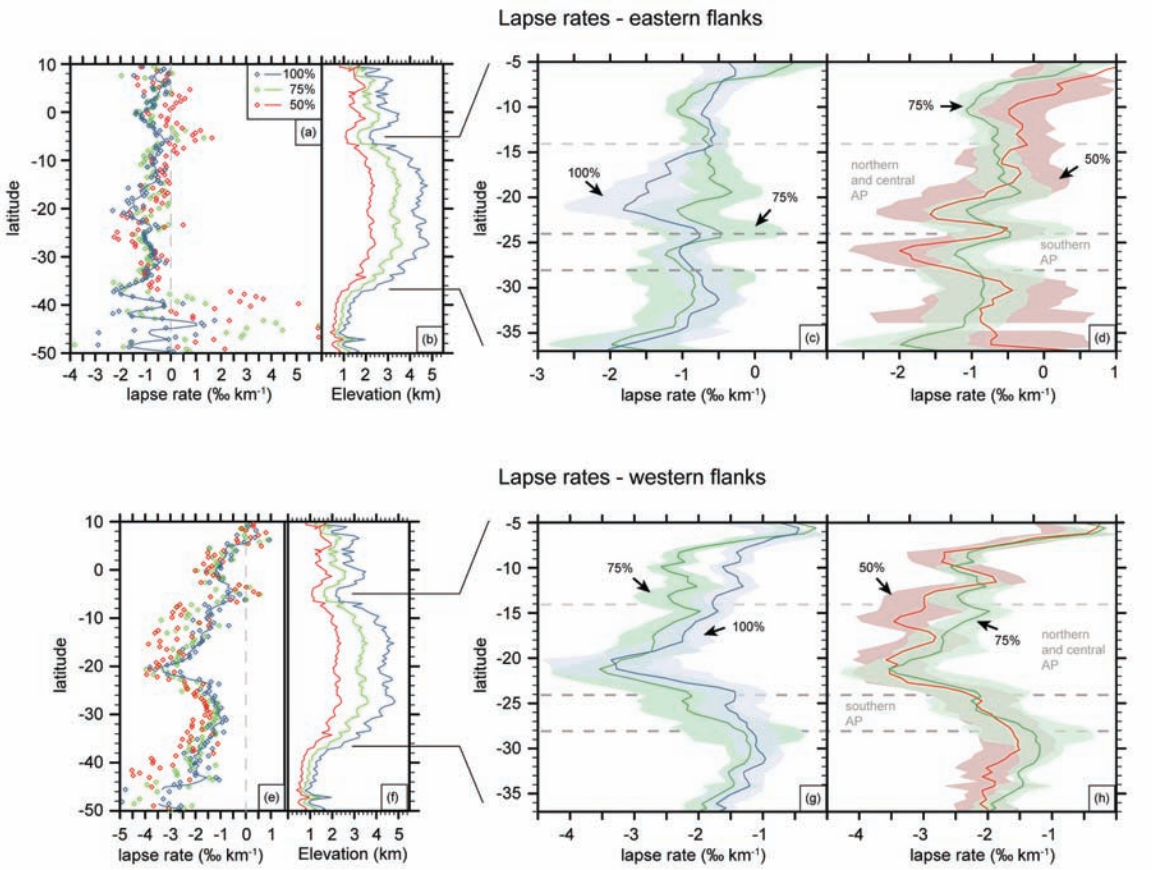

Figure 4.2: Simulated isotopic lapse rates along the eastern (a-d) and western (e-g) flank of the Andes for different height scenarios (100%, 75%, and 50% of the modern elevation). (a) All calculated lapse rates (‰ km^{-1}) between 10°N and 50°S. Diamonds represent simulated lapse rates for each latitudinal transect; colored lines represent the 2 degree running average through the data. The gray dashed line highlights the zero line. (b) Maximum elevation along the Andes for different simulation scenarios. (c-d) Isotopic lapse rates (‰ km^{-1}) between 5° and 35°S. Solid lines represent mean isotopic lapse rates, the shaded area is the 1σ standard deviation calculated from the 10 year simulation. Gray dashed lines represent borders of the northern and central Andean Plateau (AP), and the southern part of the AP, respectively. Despite large variations in annual isotopic lapse rates, we suggest that because the changes in mean isotopic lapse rates reflect large-scale climatological changes associated with surface uplift they are instructive of past lapse rate changes. (e, f, g, h) Same as a, b, c, and d, but for the western flank of the Andes.

4.4.2 Sensitivity of $\delta^{18}O_p$ to surface uplift

In comparison to the modern, $\delta^{18}O_p$ in lower-elevation simulations is substantially larger (less depleted, >7‰) over regions of high elevation, but smaller (more depleted) by approximately 2-3‰ in the lowlands (compare Fig. 4.1b-e). A decrease

in Andean $\delta^{18}O_p$ with increasing elevation is expected from the altitude effect. However, the decrease in $\delta^{18}O_p$ over the central Andes (5-30°S) with Andean surface uplift is not systematic with an increase in surface elevation, but differs in magnitude and timing across the Andean Plateau (AP). For example, the southern AP (24-28°S) experiences the largest decline in $\delta\ ^{18}O_p$ (3-4‰) when the Andes are uplifted from 50 to 75% of their modern elevation, while the northern/central AP region (14-24°S) experiences the largest decrease (>5‰) when Andean surface elevations increase from 75 to 100% (Fig. 4.1b-e). To understand the isotopic response to surface uplift on regional scales, in the following we discuss the progressive $\delta^{18}O_p$ changes when the Andes are uplifted from 50 to 100% of their modern heights. Our analysis is focused on regions where the changes in the isotopic concentration are significant at the 80% confidence level (Fig. 4.1).

Uplift of the Andes from 50 to 75% of modern elevations leads to a decrease in $\delta^{18}O_p$ of ∼2-4‰ over the high elevation Andes (Fig. 4.1d), while the isotopic composition along the eastern flank slightly increases. One exception is the southern AP region, where $\delta^{18}O_p$ becomes more depleted at high and low elevations. The overall decrease in $\delta^{18}O_p$ over the high Andes is related to the initiation/strengthening of the South American low-level jet (LLJ). A strong LLJ intensifies convergence, orographic lifting, and latent heat release, which fuels convection and convective condensation. Greater precipitation along the eastern Andean flank (Fig. 4.3d) results in stronger isotopic fractionation through Rayleigh distillation over the high Andes. Along the eastern flank of the southern AP, the establishment of the LLJ also intensifies transport of isotopically depleted moisture from the north. This isotopically depleted vapor replaces relatively enriched vapor sourced from the South Atlantic region. However, south of 30°S, where the LLJ terminates, $\delta^{18}O_p$ becomes

more enriched in the Andean foreland due to a southward shift and intensification of the subtropical high. The changes in position and magnitude of the subtropical high cause an enhanced influx of $\delta^{18}O_p$ enriched air masses from the subtropical region and lower influx from the isotopically more depleted mid-latitude regions.

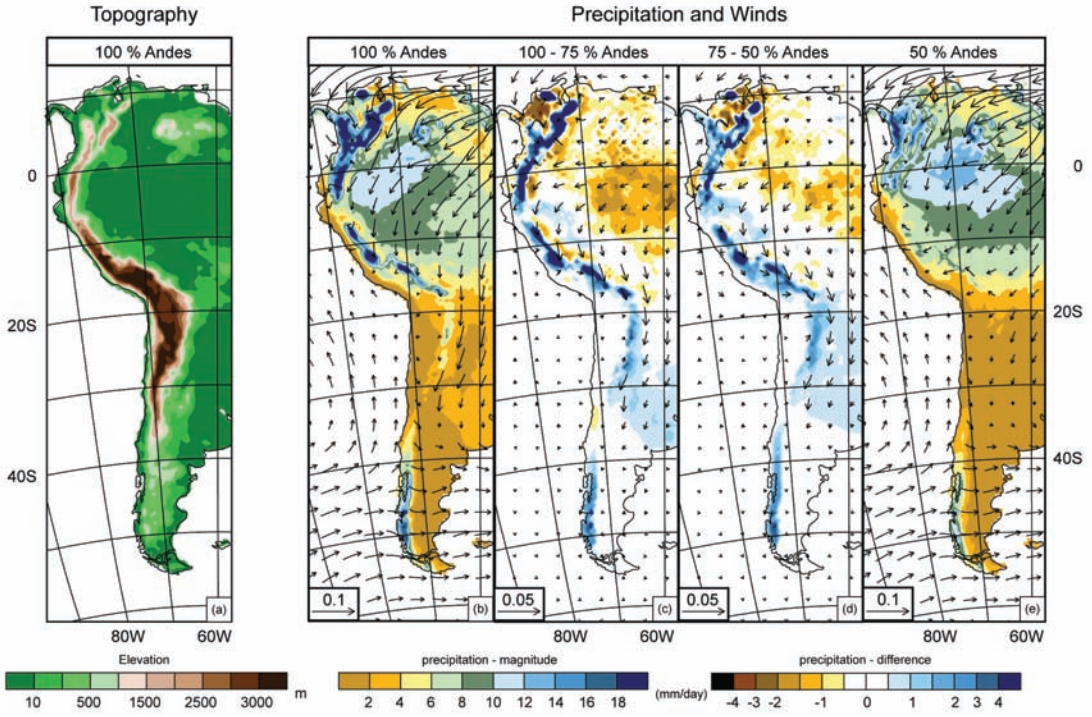

Figure 4.3: Simulated precipitation (mm day^{-1}) and low-level (850 mb) circulation over the Andes. (a) Present-day topography used in the model for 100% Andes simulations. (b-e) Changes in precipitation and low-level wind pattern (m s^{-1}) between 50% and 100% Andean heights. (e) Absolute values of precipitation and wind for 50% Andean height simulations, (d) difference in precipitation and wind between 75 and 50% Andes, (c) difference in precipitation and wind between 100 and 75% Andes, and (b) absolute precipitation and wind values for simulations with 100% Andes, respectively.

Uplift of the Andes from 75 to 100% of modern elevation causes a substantial (up to 6‰) decrease in $\delta^{18}O_p$ over the AP (Fig. 4.1c), and an increase in $\delta^{18}O_p$ by ∼3‰ along the eastern flank. These changes are related to weaker convergence over the Amazon Basin and the amplification of the LLJ. A reduction in moisture convergence over the Amazon Basin, associated with a strengthening in the low-pressure system over the Andes that draws in the moisture from the Amazon Basin, leads

to a decrease in precipitation (Fig. 4.3c) and an increase in $\delta^{18}O_p$ over the (south-) western part of the Amazon Basin (Fig. 4.1c). Northeasterly winds transport this enriched vapor from the Amazon Basin to the Andean lowlands and increase $\delta^{18}O_p$ compositions along the eastern Andean flank. Moreover, the stronger LLJ causes enhanced convergence and rainout that leads to stronger isotopic fractionation through Rayleigh distillation over the high Andes. Interestingly, $\delta^{18}O_p$ increases by 1-2‰ over the high Andes between 7 and 14°S. In this region, isotopic enrichment at high elevations is consistent with enhanced transport of isotopically enriched vapor from the South Pacific as a consequence of enhanced upward motion along the western flank. This upward motion is associated with intensified upper-level convergence over the Amazon Basin, which causes localized upper-level divergence over the western Andean flanks.

4.4.3 Sensitivity of isotopic lapse rates to surface uplift

The non-uniform $\delta^{18}O_p$ response to surface uplift over relatively small spatial scales impacts local isotopic lapse rates at different Andean heights. Due to interannual climate variability, annual oxygen isotopic lapse rates are variable and have large standard deviations from 10-year mean lapse rates (Fig. 4.2c-d, and 4.2g-h). Nevertheless, we suggest that because the changes in mean isotopic lapse rates reflect large-scale climatological changes associated with surface uplift they are instructive of past lapse rate changes.

When the Andes are uplifted from 50 to 75% of modern elevation, lapse rates along the eastern flank increase north of the AP (7-11°S) by > 0.5‰ km^{-1} (Fig. 4.2d) due to the simultaneous increase in $\delta^{18}O_p$ along the flank and decrease in $\delta^{18}O_p$ over the plateau region. Isotopic lapse rates decrease by $\sim$0.7‰ km^{-1} across the southern AP

(Fig. 4.2d), where $\delta\ ^{18}O_p$ becomes more depleted at high and low elevations. Along the western flank, isotopic lapse rates decrease with increasing elevation (Fig. 4.2h).

When the Andes are uplifted from 75 to 100% of modern elevations lapse rates along the eastern flank increase over the northern/central AP (up to 0.8‰ km^{-1}, Fig. 4.2c). The significant change in isotopic lapse rates is related to the strong decrease in $\delta^{18}O_p$ over most parts of the AP and simultaneous increase in $\delta^{18}O_p$ along the eastern Andean flank. North of this region (7-11°S), lapse rates slightly decrease (by 0.1-0.3‰ km^{-1}, Fig. 4.2c) due to an increase in $\delta^{18}O_p$ over the plateau region. Along the western flank, isotopic lapse rates significantly decrease north of the AP by almost 1‰ km^{-1} (Fig. 4.2g), most likely due to a reduction in the westward transport of continental air masses over the Andes (Fig. 4.3b). The Andes effectively block the moisture from the east, hindering transport of relatively light $\delta^{18}O_p$ from the continent.

4.5 Discussion

4.5.1 Effects of $\delta^{18}O_p$ and lapse rate changes on paleoaltimetry estimations

Our results demonstrate that $\delta^{18}O_p$ and isotopic lapse rates change substantially in response to regional climate change associated with Andean surface uplift. These findings are consistent with results from a lower resolution atmospheric global general circulation model that predicts non-uniform changes in $\delta^{18}O_p$ for Andean surface uplift from 0 to 50% and 50 to 100% of modern elevations, respectively (Poulsen et al., 2010). Here, we refine previous conclusions and identify an elevation threshold of 75% of modern Andean heights (∼3000 m) that leads to dramatic changes in the $\delta^{18}O_p$ along the Andes due to the strengthening of the LLJ and associated increase in rainout and Rayleigh distillation. The ≥5‰ depletion in $\delta^{18}O_p$ across the north-

ern/central AP associated with the amount effect noticeably exceeds the expected ∼1.5 to 2‰ $\delta^{18}O_p$ change related to the modern altitude effect. North of the AP, a ∼1.5‰ increase in $\delta^{18}O_p$ related to lower- and upper-level atmospheric circulation changes is opposite to the expected altitude effect. These results demonstrate the sensitivity of isotopic compositions to factors other than elevation change and highlight the large uncertainties associated with paleoelevation reconstructions solely based on shifts in the $\delta^{18}O_p$ paleorecord.

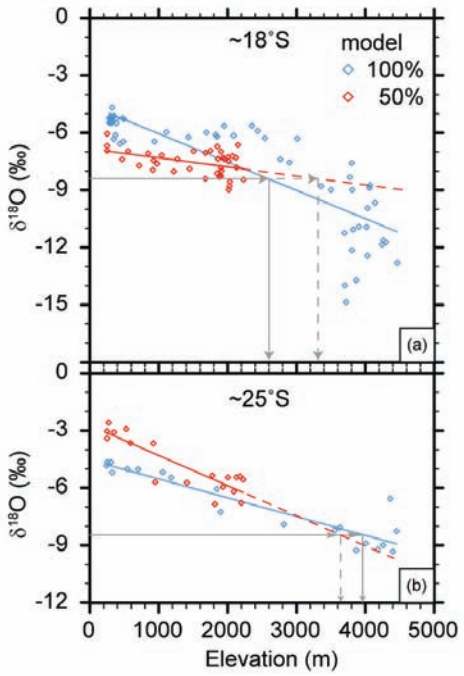

Figure 4.4: Examples of $\delta^{18}O_p$ - altitude relationships for model simulations with 100% and 50% Andean elevations across the Andean Plateau. Gray lines highlight the uncertainties in estimating paleoelevations from modern lapse rates. (a) $\delta^{18}O_p$ - altitude relationship at approximately 18°S indicates larger modern lapse rates than 50% elevation lapse rates. Using a modern lapse rate to infer paleoelevations results in an underestimation of altitude. (b) Examples for $\delta^{18}O_p$ - altitude relationship at approximately 25°S with modern lapse rates smaller than 50% elevation lapse rates. Using a modern lapse rate to infer paleoelevations results in an overestimation of altitude.

Because the $\delta^{18}O_p$ response to surface uplift varies across the Andes, isotopic lapse rates also vary spatially with Andean elevation gain. Figure 4.4 shows the $\delta^{18}O_p$ - altitude relationship for the 100% and 50% Andean elevation simulations at ∼18°S

and 25°S, respectively, and indicates the uncertainty in estimating paleoelevations. For example, in the northern Andes (Fig. 4.4a) using the modern lapse rate, a $\delta^{18}O_p$ composition of -8.5‰ would be interpreted to reflect an elevation of ∼2600 m, while using an isotopic lapse rate calculated for the 50% scenario would lead to an altitude of ∼3400 m. In contrast, in the southern AP a stable isotope signal of -8.5‰ would be interpreted to reflect an elevation of ∼4000 m by using the modern lapse rate, while the 50% lapse rate would suggest an elevation of ∼3600 m. This example shows that depending on the location, using a modern lapse rate to estimate paleoelevations can lead to either an under- or overestimation of past elevations.

4.5.2 Miocene carbonate δ^{18}O response to Andean surface uplift

In the central Andes, a 3-4‰ depletion of $\delta^{18}O$ in ancient carbonate nodules has been interpreted to reflect changes in Andean surface elevation of ∼2.5 km since the late Miocene (Garzione et al., 2006). This interpretation is based on using a modern isotopic lapse rate of approximately -1.4 to -2.3‰ km^{-1} (Gonfiantini et al., 2001) and suggests that the oldest carbonate samples (11.5 to 10.3 Ma) indicate paleoelevations of less than 1500 m and the youngest samples (6.8 to 5.5 Ma) represent modern elevations of ∼3800 m. However, our results lead to an alternate interpretation.

Figure 4.5 shows the $\delta^{18}O_p$ - altitude relationship for model simulations with 100%, 75%, and 50% Andean heights, as well as modern $\delta^{18}O_p$ from climate stations and isotopic compositions derived from the ancient carbonate nodules that were sampled on the AP (Garzione et al., 2006). Model simulations and modern isotope data from climatological stations suggest that isotopic compositions lower than -10‰ generally reflect fractionation processes at elevations above 3000 m (Fig. 4.5). To compare proxy $\delta^{18}O_{PDB(PeeDeeBelemnite)}$ from carbonates with isotopic compositions

in rainwater ($\delta^{18}O_p = \delta^{18}O_{SMOW(StandardMeanOceanWater)}$), we calculate the $\delta^{18}O_{SMOW}$ of water in equilibrium with the carbonates. The fractionation of oxygen into the mineral calcite depends on the temperature during mineral formation. We estimate the $\delta\ ^{18}O_{SMOW}$ of water from which the carbonates grew based on the reported $\delta^{18}O_{PDB}$ of the carbonates, the simulated temperature at the sample location using our three elevation scenarios (50, 75, and 100%), and the equilibrium water-calcite oxygen isotopic fractionation factor (Kim and O'Neil, 1997). We note that changes in global temperature and ice volume during the Miocene could impact our results. Simulated $\delta^{18}O_p$ would most likely increase by $\sim$1‰ due to the combining effects of warmer temperature conditions related to higher atmospheric CO_2 (<2‰ increase in $\delta^{18}O_p$) and smaller ice volumes (<1‰ decrease in $\delta^{18}O_p$) (Poulsen et al., 2007; Zachos et al., 2001). $\delta^{18}O_{SMOW}$ compositions are 0.5‰ more enriched when calculated with 2°C higher carbonate growth temperatures. Thus, existing discrepancies between model results and observations may increase by 0.5‰, but do not alter our general interpretations drawn below.

Figure 4.5a shows model-temperature derived $\delta^{18}O_{SMOW}$ values for the oldest carbonate samples plotted as a function of our hypothetical elevation scenarios (50, 75, and 100% of modern). The temperature derived $\delta^{18}O_{SMOW}$ is depleted in comparison to both observed and simulated $\delta^{18}O_p$ for lower elevations; and is most consistent with a high-elevation scenario (Fig. 4.5a). The $\delta\ ^{18}O_{SMOW}$ composition of the ancient carbonate nodules is typically less than -10‰ suggesting a paleoelevation >3000 m. Similarly, $\delta^{18}O_{SMOW}$ compositions for carbonate nodules dated for 10.3 to 6.8 Ma suggest high elevations when compared to model results and modern observations (Fig. 4.5b). Note that Fig. 4.5b includes $\delta^{18}O_{SMOW}$ values for all 10.3 to 6.8 Ma old data reported by Garzione et al. (2006), although they interpret most of the

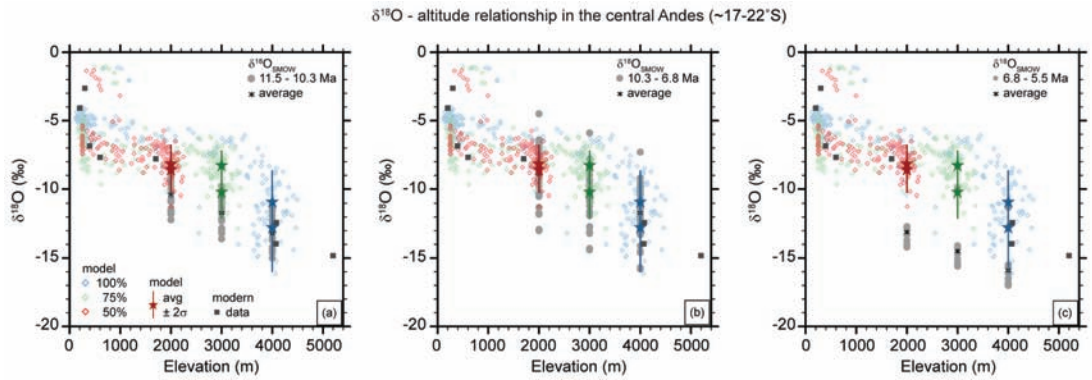

Figure 4.5: $\delta^{18}O_p$ - altitude relationship for the central Andean Plateau from model results (50, 75, and 100% of modern Andean elevations) and observations. Modern data are averaged data from meteorological stations (GNIP); $\delta^{18}O_{SMOW}$ are re-calculated from Garzione et al. (2006). Gray dots represent $\delta^{18}O_{SMOW}$ values (‰) of meteoric water in equilibrium with carbonates based on the simulated temperature at the sample location using our three elevation scenarios, and plotted at the appropriate elevations (2000, 3000, and 4000 m, respectively). Gray stars represent the average $\delta^{18}O_{SMOW}$. Colored stars represent the averaged simulated $\delta^{18}O_p$ compositions and 2σ variation for the appropriate elevation ($\pm$100 m) for annual (more enriched) and summer (more depleted) conditions. (a) $\delta^{18}O_{SMOW}$ represents compositions in carbonate nodules dated between 11.8 and 10.3 Ma. (b) Same as a, but for 10.3 to 6.8 Ma old carbonates. Note that we recalculated $\delta^{18}O_{SMOW}$ for all carbonates samples reported in Garzione et al. (2006) although they excluded the more enriched values in their analysis of paleoelevations due to possible evaporation effects. (c) Same as a, but for carbonates dated between 6.8 and 5.5 Ma.

more enriched data to reflect evaporative enrichment of ^{18}O during lacustrine deposition. However, our model results suggest a wide range of $\delta^{18}O^p$ compositions at high elevations that are consistent with the $\delta^{18}O_{SMOW}$ of all carbonate samples (Fig. 4.5b).

The $\delta^{18}O_{SMOW}$ compositions for the youngest carbonate samples are strongly depleted and plot at the lower end of modern annual $\delta^{18}O_p$ values (Fig. 4.5c). One reason for the mismatch might be a seasonal bias in pedogenic carbonate formation. Seasonality of carbonate formation is still uncertain, but it has been suggested that in most settings carbonates mainly form during warm periods (Breecker et al., 2009; Quade et al., 2007). Thus, Andean carbonates most likely acquire their isotopic signature during the rainy season and, therefore, reflect more depleted $\delta^{18}O_p$. Interestingly, seasonality significantly impacts $\delta^{18}O_p$ at high elevations, but $\delta^{18}O_p$

compositions at low elevations (e.g. in the 50% experiment) only experience minor changes (Fig. 4.5). Integrating all available data indicates that the stable isotopic composition of the ancient carbonate nodules could be interpreted to represent paleoelevations between 3000 and 4000 m and does not need to reflect fast and recent surface uplift. This interpretation is consistent with our model prediction that $\delta^{18}O_p$ decreases by over 5‰ when the Andes are uplifted from 75% to 100% modern elevations (Fig. 4.1c).

4.5.3 Miocene Δ_{47} clumped isotope response to Andean surface uplift

The hypothesis of fast and recent AP uplift is also based on reconstructed temperature changes and inferred paleoelevation reconstructions from paleobotany (Gregory-Wodzicki, 2000) and clumped-isotope (Δ_{47}) thermometry (Eiler et al., 2006; Ghosh et al., 2006b). In the latter case, clumped-isotope thermometry is used to estimate carbonate growth temperatures independently of the $\delta^{18}O$ of waters from which they formed (Ghosh et al., 2006a) and compare estimated growth temperature to a known altitudinal gradient in surface temperature. On the AP, late Miocene carbonates show a temperature decline of 15.8°C that has been interpreted to reflect 3400 ± 600 m of Andean surface uplift between 10.3 and 6.7 Ma based on the modern adiabatic lapse rate for the tropics of ∼5°C km^{-1} (Gonfiantini et al., 2001). However, the interpretation of Δ_{47} and inferred soil paleotemperatures are still a matter of debate (Eiler et al., 2006; Sempere et al., 2006). For example, Fig. 4.6a and 4.6b show the modern relationship between temperature - altitude and temperature - $\delta^{18}O$ for simulated and observed data from the central Andes. Δ_{47}-estimated AP temperatures for the youngest carbonate samples (interpreted to reflect near-modern elevations) vary by ∼14°C (Fig. 4.6a; gray filled circles), a temperature range that is almost as large

as the temperature difference that has been interpreted to reflect >3000 m surface uplift. In addition, the estimated temperatures are mostly higher than modern temperatures found at high elevations (Fig. 4.6a). If we use the clumped-isotope derived temperatures to calculate $\delta^{18}O_{SMOW}$ of water in equilibrium with the carbonates, the clumped-isotope derived $\delta^{18}O_{SMOW}$ decreases with temperature as expected, but the absolute isotopic composition is lower than both model results and modern observations (Fig. 4.6b). Even if we assume ~1 or 2°C higher temperatures in the late Miocene due to higher atmospheric CO_2 concentrations, calculated $\delta^{18}O_{SMOW}$ are still too low for the proposed temperatures (Fig. 4.6b).

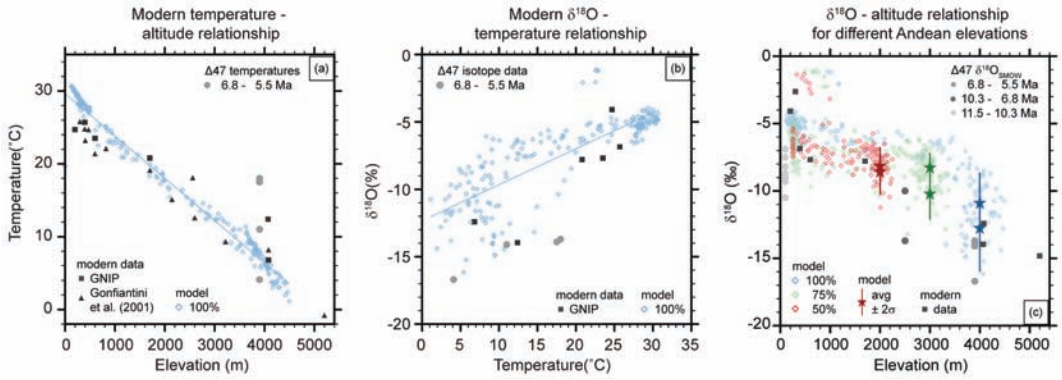

Figure 4.6: Temperature (°C), isotopes (‰), and altitude (m) relationships for the central Andes. Δ_{47} clumped isotope data are from Ghosh et al. (2006b); modern data are averaged data from meteorological stations (GNIP) and from Gonfiantini et al. (2001). (a) Modern temperature - altitude relationship for simulated and observed data. Δ_{47} temperature represent Δ_{47}-estimated temperatures for carbonate samples interpreted to reflect modern elevations (Ghosh et al., 2006b). (b) Modern δ ^{18}O - temperature relationship for simulated and observed data. Gray circles represent $\delta^{18}O_{SMOW}$ compositions calculated with Δ_{47}-estimated temperatures. (c) $\delta^{18}O_p$ - altitude relationship for model simulations with 50, 75, and 100% of modern Andean elevations and previously reported clumped-isotope derived δ $^{18}O_{SMOW}$ values from late Miocene Andean carbonates (Ghosh et al., 2006b) plotted against the temperature-inferred paleoelevation.

Fig. 4.6c shows the δ^{18}O - altitude relationship for model simulations with 100, 75, and 50% Andean elevations and previously reported $\delta^{18}O_{SMOW}$ values from late Miocene Andean carbonate samples calculated with clumped-isotope derived paleotemperatures (Ghosh et al., 2006b) plotted against the temperature-inferred paleoelevation. Similar to our previous results (see Fig. 4.5) the clumped-isotope derived

$\delta^{18}O_{SMOW}$ are systematically lower than simulated and observed $\delta^{18}O$ at elevations below 3000 m (Fig. 4.6c). We conclude that clumped-isotope derived temperatures are too high and that the low $\delta^{18}O$ compositions in ancient carbonates reflect higher elevations than previously interpreted.

4.6 Conclusions

In conclusion, we find that the Late Miocene change in $\delta^{18}O$ is most likely a combination of surface uplift and associated regional climate change. In comparison with our model results and modern $\delta^{18}O$ records from meteorological stations, we suggest that the 3-4‰ change in $\delta^{18}O$ in ancient carbonate nodules reflects an increase in precipitation and Rayleigh distillation during Andean surface uplift from 75 to 100% of modern elevations. The reasons for this conclusion are:

(1) Model simulations and modern isotope data from climatological stations suggest that isotopic compositions lower than -10‰ generally reflect fractionation processes at elevations above 3000 m. The $\delta^{18}O_{SMOW}$ composition of the ancient carbonate nodules is generally more depleted than -10 ‰ suggesting a paleoelevation of above 3000 m.

(2) Our model results indicate that $\delta^{18}O_p$ decreases by >5‰ with AP surface uplift from 75% to 100% of modern elevations due to changes in the low-level (850 mb) atmospheric circulation and precipitation. This isotopic depletion accounts for the entire change in the isotopic composition of carbonate nodules between 10 and 6 Ma. This result is consistent with the assumption that the soil $\delta^{18}O$ represents a paleoelevation of above 3000 m (which is equivalent to 75% Andes).

(3) Carbonate growth temperatures derived from clumped-isotope thermometry

show a large variability that is not completely understood and may reflect processes other than adiabatic cooling. In addition, the calculated $\delta^{18}O_{SMOW}$ values are inconsistent with low elevations, but are consistent with our new interpretation of Miocene Andean elevations of >3000 m.

(4) Isotopic lapse rates have a large interannual variability that causes large uncertainties in the mean lapse rate. Interpretations of paleo proxy data only based on short-term observations of modern isotopic lapse rates may not represent mean conditions. Moreover, we demonstrate that isotopic lapse rates substantially change with surface uplift and can lead to substantial misinterpretations of paleoelevations.

4.7 Acknowledgments

This work was supported by grants to C.J.P. and T.A.E. from NSF (EAR Awards 0738822 and 0907817) and the University of Michigans Graham Environmental Sustainability Institute. C.J.P. also received support from the Alexander von Humboldt Foundation. We thank K.C. Lohmann for assistance in recalculating oxygen isotopes.

Bibliography

Alpers, C. N. and Brimhall, G. H. Middle Miocene climate change in the Atacama Desert, northern Chile: Evidence from supergene mineralization at La Escondida. *Geological Society of America Bulletin*, 100:1640 – 1656, 1988.

Barnes, J. B. and Ehlers, T. End member models for Andean Plateau uplift. *Earth Science Reviews*, 97(1-4):105–132, 2009.

Breecker, D., Sharp, Z. and MacFadden, L. Seasonal bias in the formation and stable isotpic composition of pedogenic carbonate in modern soils from central New Mexico, USA. *GSA Bulletin*, 121(3-4):630 – 640, 2009.

Chamberlain, C. P., Poage, M., Craw, D. and Reynolds, J. Topographic development of the Southern Alps recorded by the isotopic composition of authigenic clay minerals, South Island, New Zealand. *Chemical Geology*, 155:279 – 294, 1999.

Drummond, C. N., Wilkinson, B. H., Lohmann, K. C. and Smith, G. R. Effect of regional topography and hydrology on the lacustrine isotopic record of Miocene paleoclimate in teh Rocky Mountains. *Palaeogeography, Palaeoclimatology, Palaeoecology*, 101:67 – 79, 1993.

Ehlers, T. and Poulsen, C. J. Influence of Andean uplift on climate and paleoaltimetry estimates. *Earth and Planetary Science Letter*, 281:238–248, 2009.

Eiler, J., Garzione, C. N. and Ghosh, P. Response to Comments on "Rapid uplift of the Altiplano revealed through 13C-18O bonds in paleosol carbonates". *Science*, 314:760c, 2006.

Garreaud, R., Molina, A. and Farias, M. Andean uplift, ocean cooling and Atacama hyperaridity: A climate modeling perspective. *Earth and Planetary Science Letter*, 292:39 – 50, 2010.

Garzione, C. N., Hoke, G., Libarkin, J. C., Withers, S., MacFadden, B., Eiler, J., Ghosh, P. and Mulch, A. Rise of the Andes. *Science*, 230(1304):doi:10.1126/science.1148615, 2008.

Garzione, C. N., Molnar, P., Libarkin, J. and MacFadden, B. Rapid late Miocene rise of the Bolivian Altiplano: Evidence for removal of mantle lithosphere. *Earth and Planetary Science Letters*, 241:543–556, 2006.

Ghosh, P., Adkins, J., Affek, H., Balta, B., Guo, W., Schauble, E. A., Schrag, D. and Eiler, J. M. 13C-18O bonds in carbonate minerals: A new kind of paleothermometer. *Geochimica et Cosmochimica Acta*, 70:1439 – 1456, 2006a.

Ghosh, P., Garzione, C. and Eiler, J. Rapid uplift of the Altiplano revealed through 13C-18O bonds in paleosol carbonates. *Science*, 311:511 – 515, 2006b.

Gonfiantini, R., Roche, M.-A., Olivry, J.-C., Fontes, J.-C. and Zuppi, G. M. The altitude effect on the isotopic composition of tropical rains. *Chemical Geology*, 181:147 – 167, 2001.

Hoffmann, G., Werner, M. and Heimann, M. Water isotope module of the ECHAM atmospheric general circulation model: A study on timescales from days to several years. *Journal of Geophysical Research*, 103(D14):16871 – 16896, 1998.

Insel, N., Poulsen, C. J. and Ehlers, T. A. Influence of the Andes mountains on South American moisture transport, convection, and precipitation. *Climate Dynamics*, pages doi:10.1007/s00382–009–0637–1, 2009.

Insel, N., Poulsen, C. J., Sturm, C. and Ehlers, T. A. Climate controls on temporal and spatial variability of andean precipitation d18O. *Climate Dynamics*, review.

Kim, S.-T. and O'Neil, J. R. Equilibrium and nonequilibrium oxygen isotope effects in synthetic carbonates. *Geochimica et Cosmochimica Acta*, 61(16):3461 – 3475, 1997.

Picard, D., Sempere, T. and Plantard. Direction and timing of uplift propagation in the Pervian Andes dedcued from molecular phylogenetics of highland biotaxa. *Earth and Planetary Science Letter*, 271:326 – 336, 2008.

Poage, M. and Chamberlain, C. P. Empirical relationships between elevation and the stable isotope composition of precipitation and surface waters: consideration for studies of paleoelevation change. *American Journal of Sciences*, 301:1 – 15, 2001.

Poulsen, C. J., Ehlers, T. and Insel, N. Onset of convective rainfall during gradual late Miocene rise of the central Andes. *Science*, page doi:10.1126/science.1185078, 2010.

Poulsen, C. J., Pollard, D. and White, T. General circulation model simulation of the d18O content of continental precipitation in the middle Cretaceous: A model-proxy comparison. *Geology*, 35:191 – 202, 2007.

Quade, J., Garzione, C. and Eiler, J. Paleoelevation reconstructions using pedogenic carbonates. *Reviews in Mineralogy and Geochemistry*, 66:53–87, 2007.

Rech, J. A., Currie, B. S., Michalski, G. and Cowan, A. M. Neogene climate change and uplift in the Atacama Desert, Chile. *Geology*, 34(9):761–764, 2006.

Schlunegger, F., Kober, F., Zeilinger, G. and von Rotz, R. Sedimentology-based reconstructions of paleoclimate changes in the Central Andes in response to the uplift of the Andes, Arica region between 19 and 21?S latitude, northern Chile. *International Journal of Earth Sciences*, pages doi:10.1007/s00531–010–0572–8, 2010.

Sebrier, M., Lavenu, A., Fornari, M., Soulas, J. P. and Anonymous. Tectonics and uplift in Central Andes (Peru, Bolivia and northern Chile) from Eocene to present. In *Seminaire; Geodynamique des Andes centrales. Seminar on Geodynamics of the Central Andes*, volume 3, pages 85–106. Office de la Recherche Scientifique et Technique Outre-Mer (ORSTOM), Bondy, 1988.

Sempere, T., Hartley, A. J. and Roperch, P. Comment on "Rapid uplift of the Altiplano revealed through 13C-18O bonds in paleosol carbonates". *Science*, 314:760, 2006.

Siegenthaler, U. and Oeschger, H. Correlation of 18O in precipitation with temperature and altitude. *Nature*, 285:314 – 317, 1980.

Stern, L. A. and Blisniuk, P. M. Stable isotope composition of precipitation across the southern Patagonian Andes. *Journal of Geophysical Research*, 107(D23)(4667):doi:10.1029/2002JD002509, 2002.

Sturm, C., Hoffmann, G. and Langmann, B. Simulation of the stable water isotopes in precipitation over South America: Comparing regional to global circulation models. *Journal of Climate*, 20:3730 – 3750, 2007a.

Sturm, C., Vimeux, F. and Krinner, G. Intraseasonal variability in South America recorded in stable water isotopes. *Journal of Geophysical Research*, 112:doi:10.1029/2006JD008298, 2007b.

Sturm, K., Hoffmann, G., Langmann, B. and Stichler, W. Simulation of d18O in precipitation by the regional circulation model REMOiso. *Hydrological Processes*, 19:3425 – 3444, 2005.

Vuille, M., Bradley, R. S., Werner, M., Healy, R. and Keimig, F. Modeling d18O in precipitation over the tropical Americas: 1. Interannual variability and climate controls. *Journal of Geophysical Research*, 108(D6):doi:10.1029/2001JD002038, 2003.

Zachos, J., Pagani, M., Sloan, L., Thomas, E. and Billups, K. Trends, rhythms, and aberrations in global climate 65 Ma to present. *Science*, 292:686–693, 2001.

CHAPTER V

Spatial and temporal variability in denudation across the Bolivian Andes from multiple geochronometers

5.1 Abstract

We quantify spatial and temporal variations in denudation rates across the central Andean fold-thrust belt in Bolivia with particular focus on the Holocene. Measured and predicted ^{10}Be cosmogenic radionuclide (CRN) concentrations in river sediments are used to (1) calculate catchment-averaged denudation rates from 17 basins across two transects at different latitudes, and (2) evaluate the sensitivity of Holocene climate change on the denudation history recorded by the CRN data. Estimated denudation rates vary by two orders of magnitude from 0.04 to 1.93 mm yr^{-1} with mean values of 0.40±0.29 mm yr^{-1} in northern Bolivia and 0.51±0.50 mm yr^{-1} in the south. Results demonstrate no statistically significant correlation between denudation rates and morphological parameters such as relief, slope or drainage basin size. In addition, the CRN- derived denudation rates do not reflect present-day latitudinal variations in precipitation. Comparison to ∼130 previously published denudation rates calculated over long (thermochronology-derived; >10^6 yrs), medium

Official citation:
Insel, N., T.A. Ehlers, M. Schaller, J.B.Barnes, S. Tawackoli, C.J. Poulsen (2010). Spatial and temporal variability in denudation across the Bolivian Andes from multiple geochronometers. *Geomorphology*, doi:10.1016/j.geomorph.2010.05.014

(CRN-derived; 10^2−10^4 yrs), and short timescales (sediment flux- derived; 10^1 yrs) indicate temporal variations in denudation rates that increase between 0 and 200% over the last ∼5 kyrs. CRN modeling results suggest that the CRN-derived denudation rates may not be fully adjusted to wetter climate conditions recorded in the central Andes since the mid-Holocene. We conclude that large spatial variability in CRN denudation may be due to local variations in tectonics (e.g. faulting), while large temporal variability in denudation may be due to temporal variations in climate.

5.2 Introduction

A close link between tectonics, climate, and denudation in the evolution of mountain belts has been hypothesized in a variety of modeling and observational studies (e.g., Willett, 1999; Leturmy et al., 2000; Beaumont et al., 2001; Hilley and Strecker, 2004). For example, it has been proposed that regional variations in climate may strongly influence spatial variations in denudation, thereby affecting the style and location of deformation and exhumation (e.g., Willett, 1999). The 7000 km long Andes Mountains in South America are thought to exemplify these linkages because correlations between latitudinal variations in tectonic deformation, topography, and precipitation, as well as denudation rate estimates, suggest that climate-driven denudation exerts a fundamental control on mountain evolution (e.g., Masek et al., 1994; Montgomery et al., 2001). In particular, the central Andean fold-thrust belt (∼14-26°S) is characterized by high relief and steep slopes north of 18°S that have been hypothesized to reflect high orographic precipitation and high denudation rates, while the more gentle and wider topography of the drier regions south of 18°S may reflect a tectonic landform less modified by climate and denudation (Masek et al.,

1994; Horton, 1999; Barnes et al., 2006; McQuarrie et al., 2008a). Improved quantification of the spatial and temporal variations in magnitude and mechanism of denudation across the central Andes reveals variations in denudation processes that might be related to changes in tectonics, climate, or land use, and is essential to understand the role of denudation in shaping landscapes (Gillis et al., 2006; Barnes and Ehlers, 2009).

Terrestrial denudation rates are sensitive to both tectonics and climate, but the importance of each effect is difficult to constrain. Averaged long-term ($>10^6$ yrs) denudation rates in the Bolivian Andes that are estimated from low-temperature thermochronology (e.g. apatite fission track (AFT) dating) mainly represent denudation driven by tectonic-related processes and are similar along strike (Benjamin et al., 1987; Barnes et al., 2006; Gillis et al., 2006; Safran et al., 2006; Ege et al., 2007; Barnes et al., 2008; McQuarrie et al., 2008a). Averaged medium-term (10^2-10^4 yrs) denudation rates calculated from cosmogenic radionuclides (CRN) in the northern Bolivian Andes are within the range of long-term denudation rates in the same area (Safran et al., 2005). No medium-term denudation data exist from the southern part of the Bolivian Andes. Short-term (10^1-10^2 yrs) denudation rate estimates from sediment flux data in the Bolivian Andes mirror the present-day latitudinal precipitation gradient and indicate a disparity with $\sim$3 times higher mean denudation rates in northern Bolivia ($14-18^\circ$S) compared to the south ($18-22^\circ$S) (Barnes et al., 2006). Previous studies suggest that the along-strike variability in denudation existed throughout the Holocene with an increase in denudation and north- south contrast since as early as the late Miocene ($\sim$10 Ma) (Anders et al., 2002; Safran et al., 2005; Barnes et al., 2006). Structural and thermochronometer data and basin sedimentation histories were used to infer orographically controlled and/or South American

monsoon system-related intensification of precipitation and denudation in Bolivia also in the late Miocene (McQuarrie et al., 2008a; Uba et al., 2009). This intensification could be due to plateau uplift beyond some substantial elevation threshold (Garzione et al., 2006; Ehlers and Poulsen, 2009; Insel et al., 2009; Mulch et al., 2010).

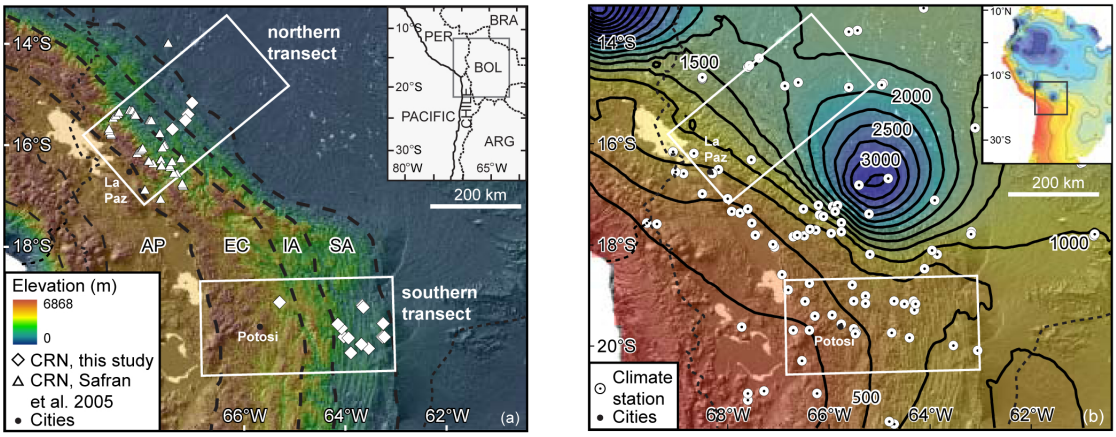

Figure 5.1: Topography, precipitation, and cosmogenic radionuclide (CRN) samples of the Bolivian Andes. (a) Shaded 90 m digital elevation model (SRTM DEM) of the Bolivian Andes showing major morphological units (AP: Altiplano, EC: Eastern Cordillera, IA: Interandean zone, SA: Subandes) and location of study area transects. CRN samples are from this study (diamonds) and Safran et al. (2005)(triangles). Small dashed lines are country borders. Elevations span ∼300−500 m in the foreland to 6800 m west of the AP. Inset shows study area location in west-central South America (modified from Barnes et al. 2008. (b) Same map showing modern precipitation distribution interpolated from the Global Historical Climatology Network climate station data (Peterson and Vose, 1997). Contour interval is 250 mm yr^{-1}. Inset shows 500 mm yr^{-1} precipitation contours for South America.

In this study, we integrate 17 new cosmogenic ^{10}Be analyses with 43 previously published CRN data (Safran et al., 2005) to quantify catchment-averaged denudation rates from the Andean fold-thrust belt in Bolivia (Fig. 5.1a). New samples were collected across two different transects in the northern (∼15°S) humid and southern (∼19°S) dry part of the Bolivian Andes (Fig. 5.1b) with a focus on the Subandes which have been uplifted since the Miocene (e.g., Barnes et al., 2008; Uba et al., 2009). These data are used to quantify (1) spatial variations in denudation by comparing CRN-derived denudation rates from the northern and southern transects,

and (2) temporal variations in denudation rates by comparing rates on different time scales. In addition, we (3) compare magnitudes of denudation with modern variations in precipitation and geomorphic indices (e.g. slope and relief). Our results complement previous work in the northern Bolivian Andes (Safran et al., 2005) and add new data from the southern Bolivian Andes to verify the strong disparity in denudation rates over time. The combination of our results with previously estimated sediment flux-derived denudation rates (Aalto et al., 2006; Barnes et al., 2006) reveal Holocene variations in denudation processes and the possible effect of climate change on radionuclide concentrations over the last ∼5 ka.

5.3 Geologic, geomorphic, and climate setting

The central Andes (14−26°S) form the widest and highest portion of the Andean Cordillera. The central Andean fold-thrust belt occupies the eastern flank of the Cordillera and is divided into four physiographic units (Fig. 5.1a) (Kley, 1996; McQuarrie, 2002): (a) the low relief, internally-drained Altiplano (AP) with an average elevation of >3 km; (b) the structurally bivergent, high elevation Eastern Cordillera (EC); (c) the Interandean zone (IA); and (d) the tectonically active Subandes (SA). The thrust belt is the result of Cenozoic crustal shortening and thickening related to subduction of the Nazca plate below the South American plate (e.g., Isacks, 1988; Sempere et al., 1990; Allmendinger et al., 1997; Jordan et al., 1997; Kley and Monaldi, 1998; Oncken et al., 2006).

The central Andes are characterized by significant along-strike contrasts in the morphology and the style of deformation that have been ascribed to strong latitudinal changes in climate and/or tectonics (Fig. 5.1)(e.g., Isacks, 1988; Masek et al., 1994;

Allmendinger et al., 1997; Horton, 1999; Montgomery et al., 2001). The high relief and narrow fold-thrust belt in the northern portion of the Bolivian Andes($\sim$14$-$18°S) is distinctive from the wide and smooth topography in the south ($\sim$18$-$22°S). Based on cross-section balancing and low-temperature thermochronology, the average vertical exhumation over the last 20 Ma is higher (4-9 km) in the north than in the south (3$-$6 km) (e.g., Barnes et al., 2006, 2008; McQuarrie et al., 2008b). Lithologies involved in the deformation and exposed today are similar north to south, ranging from Ordovician to Devonian marine siliciclastic rocks and Carboniferous to Cretaceous non-marine clastics to Cenozoic synorogenic sediments (e.g., Sempere, 1995; Sempere et al., 1997; Horton, 1998; McQuarrie, 2002). As addressed in the discussion section, the mechanical strength of these sedimentary rocks in the study area is also similar along strike (McQuarrie, 2002) implying no latitudinal variation in erodibility of the different lithologies.

The central Andes are characterized by both latitudinally and orographically enhanced changes in precipitation (e.g., Aceituno, 1988; Garreaud and Wallace, 1997; Garreaud, 2000). The large-scale atmospheric circulation over South America leads to a strong regional precipitation gradient with up to 4 m yr^{-1} rainfall north of $\sim$18°S and less than 1 m yr^{-1} south of 18°S (Fig. 5.1b). In addition, the central Andes act as a topographic barrier between the humid Amazon Basin and the more arid Pacific margin to the west. Condensation of Atlantic-derived moisture on the eastern Andean flank leads to focused orographic precipitation in the eastern part of the Andean fold-thrust belt with dry conditions on the western plateau region (Lenters and Cook, 1995; Insel et al., 2009).

5.4 Methods

5.4.1 Cosmogenic radionuclide data

Modern river sediments were collected from four catchments along a northern transect and thirteen tributaries and trunk streams in a southern transect (Fig. 5.1a, Table 5.1). In the northern transect, our CRN samples are mainly from the SA with elevations between 600 and 1400 m, with previous data focused on the high elevation sites (∼1600 to 4500 m) in the EC (Figs. 5.1a and 5.2a) (Safran et al., 2005). In the southern transect, CRN data are from basins that span a wide range of basin mean elevations from 840 to 3500 m, but again focused in the SA (Table 5.1). Drainage areas upstream of sample locations vary in size and range from 4 km^2 to 5200 km^2. Samples were collected from within the active channel, focusing on the medium to small sand size fraction.

Samples were washed, dried, and sieved to isolate the grain size fraction between 0.25 and 0.5 mm. In some cases, coarser size fractions between 0.5 and 1.0 mm were used to evaluate the effect of grain size on denudation rate (Table 5.1). Quartz was separated using standard mineral separation techniques. To eliminate possible contamination by ^{10}Be produced in the atmosphere, quartz was leached with a mixture of hydrofluoric and nitric acid. After dissolution of quartz and addition of ^{9}Be spike, Be and Al were separated by extraction and precipitation following von Blanckenburg et al. (1996). Measurements by accelerator mass spectrometry were carried out at PRIME Lab, Purdue University. Average production rates for each sample site were calculated using the 90 m SRTM DEM taking into account scaling to latitude and altitude and topographic shielding for each pixel in the DEM (Stone, 2000; Balco, 2001). We used a total production rate of 5.1 atoms g^{-1} yr^{-1} for ^{10}Be and 31.1 atoms g^{-1} yr^{-1} for ^{26}Al at sea level sites and high latitude (Stone, 2000). To

account for spallogenic and muonic production, we used spallogenic fractions of 0.978 (^{10}Be) and 0.974 (^{26}Al) contributing to the total production rate (Stone, 2000), while the remaining fraction was assigned to slow and fast muons, using a ratio of 0.53 to 0.47 (Heisinger et al., 2002). The original ICN standard (Nishiizumi et al., 2007) was used as reference standard for measurements and values of 4.62x10^{-7} yr^{-1} (^{10}Be) and 9.68x10^{-7} yr^{-1} (^{26}Al) were assigned for the decay constants, respectively. Table 5.1 lists the production rates for each basin, calculated ^{10}Be and ^{26}Al concentrations, catchment-wide denudation rates, and the corresponding errors after Schaller et al. (2001, 2002).

Ratios of ^{26}Al/^{10}Be in our samples are between 3.6 and 6.2. The range of the ratios is consistent with ^{26}Al/^{10}Be ratios from Safran et al. (2005), although the average of 4.3 is much lower than the assumed production ratio of 6.1. The catchments with lower ratios were mostly basins with Al content close to the detection limit. We interpret that sediment storage is not responsible for production ratios below 6 (see Discussion section) and assume that the lower ratios are a result of incomplete recovery of stable Al during sample processing (e.g., Safran et al., 2005).

5.4.2 Long-term denudation rates

Long-term denudation rates were estimated from previously published AFT data (Suppl. 5.1) (Barnes et al., 2006; Gillis et al., 2006; Safran et al., 2006; Barnes et al., 2008; McQuarrie et al., 2008a). We only account for samples along our two transects and AFT analyses with more than 10 grains per sample. To estimate long-term denudation rates from AFT data, we used the most straightforward method of dividing a presumed closure isotherm depth by the cooling age and assuming a linear, temporally invariant geothermal gradient. For the calculation, we assumed (1)

Table 5.1: Cosmogenic sample locations, drainage basin statistics and information for CRN-derived, basin-averaged denudation rate estimates from the central Andes in Bolivia.

Sample ID	River	Sampled latitude (°S)	Sampled longitude (°W)	Sampled altitude (m)	Drainage (km^2)	Fm age[a]	Quartz yield (%)[b]	Mean relief (m)[c]	Mean slope (%)	Mean annual precipitation (mm yr^{-1})	Mean latitude (°S)	Mean altitude (m)	Production rate(atoms $(g_{(qtz)}yr)^{-1}$)[d]		^{10}Be conc (10^4atoms $g_{(qtz)}{}^{-1}$)[e]	^{26}Al conc (10^4atoms $g_{(qtz)}{}^{-1}$)[e]	Denudation rate (mm yr^{-1})[e]	Apparent age (kyr)
Northern transect																		
N02	Rio Yucumo	15.16	67.04	263	48	Dv-Te	79	460	24	1669	15.18	618	5.26		0.52±0.06		0.83±0.11	0.99
N04	Rio Qiquibey	15.39	67.12	595	332	Cb	66	425	23	1678	15.50	1106	7.58	46.15	3.64±0.18	17.23±3.70	0.17±0.01	4.80
N04[g]		15.39	67.12	595							15.50	1106	7.58	46.15	3.47±0.12		0.18±0.01	4.57
N05	Rio Inicua	15.51	67.17	562	205	Te	34	394	23	1648	15.55	1027	7.19	43.82	5.11±0.35	31.68±4.73	0.11±0.01	7.10
N06	Rio Pequende	15.68	67.43	840	34	Dv	50	645	33	1502	15.71	1397	9.40	57.27	5.47±0.21	23.82±3.68	0.14±0.01	5.82
N06[g]		15.68	67.43	840							15.71	1397	9.40	57.27	2.77±0.15		0.24±0.02	3.43
Southern transect																		
S01[g]	Rio El Chaleno	19.79	63.26	871	4	Cb-Me	73	414	41	767	19.80	1119	7.98		2.09±0.22		0.31±0.04	2.62
S03[g]	Rio Bateon	19.79	64.03	1246	5	Dv	82	521	32	727	19.77	1504	10.57		0.96±0.05		0.90±0.06	0.91
S04	Rio Azero	19.61	64.08	1101	3763	Sil-Dv	53	621	30	670	19.67	2250	18.02		13.69±0.38		0.11±0.01	7.59
S04[g]		19.61	64.08	1101							19.67	2250	18.02		7.16±0.11		0.20±0.01	3.98
S05	Rio Canas	19.53	64.15	1374	7	Dv	26	820	41	688	19.56	2059	15.49		28.86±0.84		0.04±0.003	18.63
S05[g]		19.53	64.15	1374							19.56	2059	15.49		24.72±2.74		0.05±0.006	15.96
S06[g]	Rio Cachu Mayo	19.10	65.30	2499	1318	Me/Ord	62	514	26	581	18.92	3515	36.16		73.47±2.88		0.04±0.003	20.32
S08	Rio Saipuru	19.52	63.25	832	129	Cb-Te	85	378	19	760	19.52	1082	7.75	47.20	1.63±0.13	5.85±2.36	0.39±0.04	2.10
S09	Rio Charagua	19.79	63.23	830	152	Cb-Te	86	435	21	765	19.75	1125	8.03	48.94	1.56±0.13	5.29±2.96	0.42±0.04	1.95
S09[g]		19.79	63.23	830							19.75	1125	8.03	48.94	1.60±0.28		0.41±0.07	2.00
S10	Rio Parapeti	20.01	63.54	789	5194	Dv-Te	70	446	24	748	20.13	1437	10.56	64.30	3.02±0.17	10.82±3.41	0.28±0.02	2.86
S11	Rio Iviyeca	19.93	63.68	989	20	(Dv-)Te	54	561	31	753	19.92	1298	9.15		1.14±0.11		0.65±0.07	1.25
S12	Rio Banado	20.10	63.89	988	1036	Dv-Te	83	379	20	741	19.92	1329	9.41	57.32	2.62±0.15	13.38±3.25	0.29±0.02	2.78
S13	Rio Zapaltar	19.80	63.94	1115	52	Dv-Te	77	451	25	729	19.75	1374	9.66		1.04±0.09		0.75±0.07	1.08
S15	Rio Nancahuazu	19.17	63.66	532	3127	Dv-Te	82	342	18	742	19.54	1072	7.74	47.15	1.29±0.09	4.65±3.08	0.49±0.04	1.66
S16	Rio Saladille	19.20	63.65	575	47	Cb-Me	80	402	23	734	19.22	842	6.46		0.27±0.05		1.93±0.36	0.42

[a] Fm age: formation age; Ord Ordovician; Sil Silurian; Dv Devonian; Cb Carboniferous; Me Mesozoic; Te Tertiary.
[b] Quartz content derived from the sample material (e.g. amount of quartz in relation to other minerals within the sample.
[c] Relief is calculated by substracting the highest and lowest elevations within a circular neighborhood with 2 km in radius.
[d] Production rate is scaled to lat and lon, and corrected for topographic shielding, first value is for ^{10}Be, second value for ^{26}Al, no correction necessary for snow cover or thickness.
[e] Error on concentrations includes analytical uncertainties.
[f] Denudation rate based on ^{10}Be concentration; total error includes analytical uncertainties and calculated uncertainties for production rate that is based on an assumed 10 percent uncertainty in calculated mean altitude and size of the upstream catchment area.
[g] Grain size: 0.5-1.0 mm, all others are 0.25 -0.5 mm.

an average AFT closure temperature of 110°C, (2) average surface temperatures of 10°C for the EC, 15°C for the IA, and 23°C for the SA, and (3) previously estimated values of the geothermal gradient based on proximal borehole-measurements (Barnes et al., 2006, 2008).

The estimated geothermal gradient for the northern transect is 22±2.2 °C/km for the EC, IA, and SA, while in the southern transect we use a gradient of 27±11°C/km for the EC and the IA, and 18±5 °C/km for the SA.Where available, we estimated long-term denudation rates based on sample cooling histories quantified with inverse thermal modelling (Barnes et al., 2006; Gillis et al., 2006; Barnes et al., 2008). In these cases, instead of using the cooling age, we used the onset of the most recent rapid cooling from the best-fit thermal model to calculate denudation rates (Suppl. 5.1). We also re-calculated previously estimated long-term denudation rates from Safran et al. (2006) to make them comparable with the data above. With the smaller geothermal gradient re-calculated denudation rates are mostly the same within error as originally reported, with a few exceptions up to 0.3 mm yr^{-1} higher (compare Suppl. 5.1 and Safran et al. (2006)).

Our calculated denudation rates from thermochronometer samples are only an estimate of true denudation rates over this timescale. Temporal variations in the thermal gradient due to transient denudation, magmatism, and/or removal of overlying units with significantly different thermal conductivity could all introduce uncertainty into these estimates (Ehlers et al., 2005). Addressing these complications often requires detailed thermal modelling of sample cooling histories and various thermo-tectonic processes, an endeavour beyond the scope of this study, and poorly constrained with available data. Rather, we report long-term denudation rates with conservative uncertainties (e.g. Fig. 5.4) related to the large variability in present-day

heat flow in each physiographic unit (after Barnes et al. 2006, 2008). This approach provides an empirically-derived estimate for long-term variations in denudation rates based on known variations in the present-day thermal structure of the Andes.

5.5 Results

5.5.1 Spatial variations in CRN-derived denudation rates

Denudation rate estimates based on CRN analyses were calculated from 17 basins (Table 5.1 and Fig. 5.2). The rates vary by two orders of magnitude from 0.04 to 1.93 mm yr^{-1} and indicate apparent ages of 0.4 to 20 ka. More than 75% of the basins have an apparent age younger than 5 ka.

In the northern transect, three samples from the northern SA and one from the IA were measured (Figs. 5.2a and 5.3a). The denudation rates vary by a factor of 8 and range from 0.11 to 0.83 mm yr^{-1} over apparent ages of 1.0 to 7.1 ka (Table 5.1). The highest denudation rate observed (0.83 mm yr^{-1}) is in a small basin (N02) located along the frontal range of the SA (Figs. 5.2a and 5.3a). To the west, denudation rates are smaller with magnitudes $\sim$0.1-0.2 mm yr^{-1} (Figs. 5.2a and 5.3a). Denudation rates are similar for the SA and the IA. Because samples were only available from four basins, general trends in the denudation rates are difficult to define robustly. However, the range of denudation rates is in good agreement with CRN-derived denudation rates for basins in the EC that range between 0.04-1.34 mm yr^{-1} (Figs. 5.2a and 5.3a) (Safran et al., 2005). The mean value for all calculated CRN-derived denudation rates in the northern transect is 0.40$\pm$ 0.29 mm yr^{-1}, including published rates by Safran et al. (2005). Denudation rates for different grain sizes of the same sample do not show noteworthy differences (Table 5.1).

In the southern transect, 11 samples from the southern SA, 1 from the IA, and

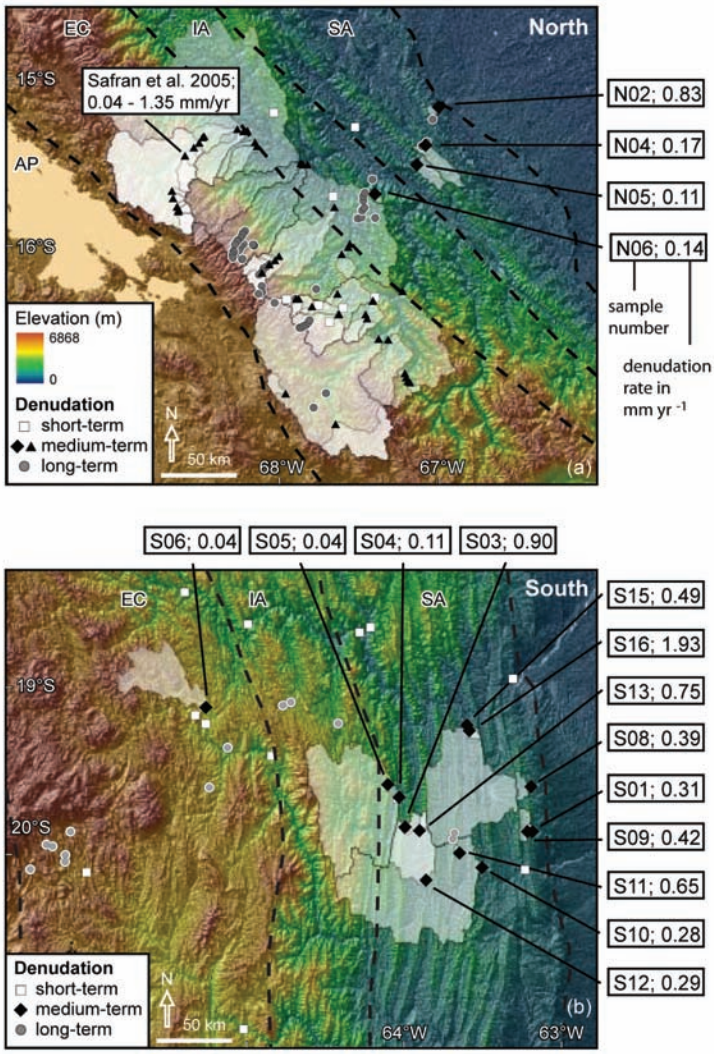

Figure 5.2: Thrust belt topography and CRN-derived denudation rates across northern and southern Bolivia in map view (see Suppl. 5.2 for short and long-term rates). Topography is the 90 m SRTM DEM with basin outlines and sample locations in the northern transect (a) and southern transect (b). Basin sizes sampled vary between 7 and 7000 km^2. Different symbols represent different timescales of denudation: short−term rates (white squares) are gauging station locations (from (Barnes et al., 2006); medium-term represents cosmogenic radionuclide (CRN)-derived denudation rates (in mm yr^{-1}) for the outlined basins in this study (black diamonds) and Safran et al. (2005) (black triangles); and longterm rates (gray circles) represent locations of apatite fission track (AFT) data (from (Barnes et al., 2006; Gillis et al., 2006; Safran et al., 2006; Barnes et al., 2008; McQuarrie et al., 2008b). AP: Altiplano, EC: Eastern Cordillera, IA: Interandean zone, SA: Subandes.

1 from the EC were measured (Figs. 5.2b and 5.3b). The denudation rates vary by two orders of magnitude from 0.04 to 1.93 mm yr^{-1} with apparent ages of 0.4 to 20.3 ka (Figs. 5.2b and 5.3b, Table 5.1). Most sampled basins are located entirely within the SA. One SA basin (S16) indicates an exceptionally high denudation rate of 1.93 mm/yr. Although the sample appears as an outlier relative to the other samples we include it in our analysis because there were no anomalous aspects of the drainage basin (e.g. recent large landslides) or abnormalities in the chemical analysis that would preclude consideration. A denudation rate of 0.1 mm yr^{-1} is calculated for a basin (S04) situated mainly in the IA. The one EC basin (S06) indicates one of the lowest denudation rates with a magnitude of 0.04 mm yr^{-1}. The mean CRN-derived denudation rate for the south is 0.51 ± 0.50 mm yr^{-1}.

5.5.2 Temporal variations in denudation rates

Transients in the denudation rates are observable when comparing rates calculated over long- (AFT-derived), medium- (CRN-derived) and short-timescales (sediment flux-derived) (Fig. 5.4). Results shown compare our CRN- derived rates with long-term rates calculated from published AFT data (see Section 5.4.2) and short-term rates from sediment gauging stations neighboring our sample locations. Sediment flux determinations include the total suspended and dissolved loads and are thought to be representative of the modern physical denudation rates (Barnes and Pelletier 2006, see also Aalto et al. 2006).

In the northern transect, short-term denudation rates were calculated from 9 sediment gauging stations that recorded sediment fluxes from drainage basins ranging in size from 270 to 67,200 km^2 (Figs. 5.2a and 5.3a) (Guyot et al., 1988; Barnes et al., 2006). Short-term denudation magnitudes vary between 0.21 and 2.49 mm yr^{-1}, with

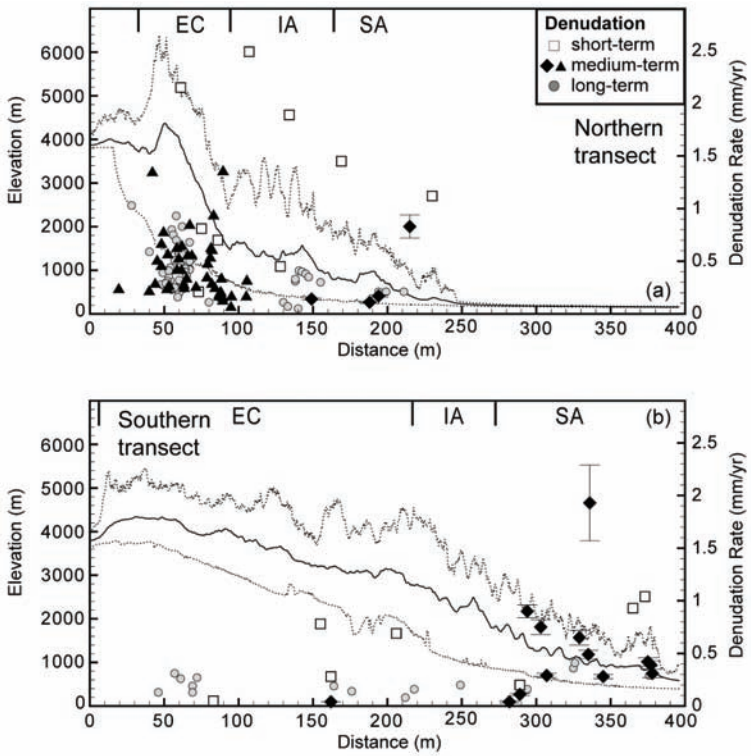

Figure 5.3: Variations in topography and denudation along the northern (a) and southern (b) transects in cross-section (see Fig. 1 for locations). The 200 km-wide swath topography profiles of maximum, minimum (dashed grey lines) and mean altitudes (solid black lines) are based on the 90 m SRTM DEM and are oriented perpendicular to the fold-thrust belt. EC: Eastern Cordillera, IA: Interandean zone, SA: Subandes. Long-, medium-, and short-term denudation rates are plotted along the profiles.

a mean denudation rate of 1.25± 0.79 mm yr^{-1} and are therefore two to three times higher than medium-term denudation rates (mean of 0.40±0.29 mm yr^{-1}, Figs. 5.3a and 5.4). AFT data from the northern transect indicate long-term denudation rates of ∼0.1-1.0 mm yr^{-1} (mean of ∼0.42±0.19 mm yr^{-1}) for the EC, 0.05-0.4 mm yr^{-1} (mean of ∼0.27±0.15 mm yr^{-1}) for the IA and 0.1-0.2 mm yr^{-1} (mean of ∼0.18± 0.06 mm yr^{-1}) for the SA (Suppl. 5.1), suggesting a decrease in long-term denudation from southwest to northeast (Fig. 5.3a). The mean denudation rate based on the AFT data for the entire transect is 0.38±0.19 mm yr^{-1} and is within error similar to the CRN-derived denudation rates (Fig. 5.4).

In the southern transect, short-term denudation rates were estimated from 7

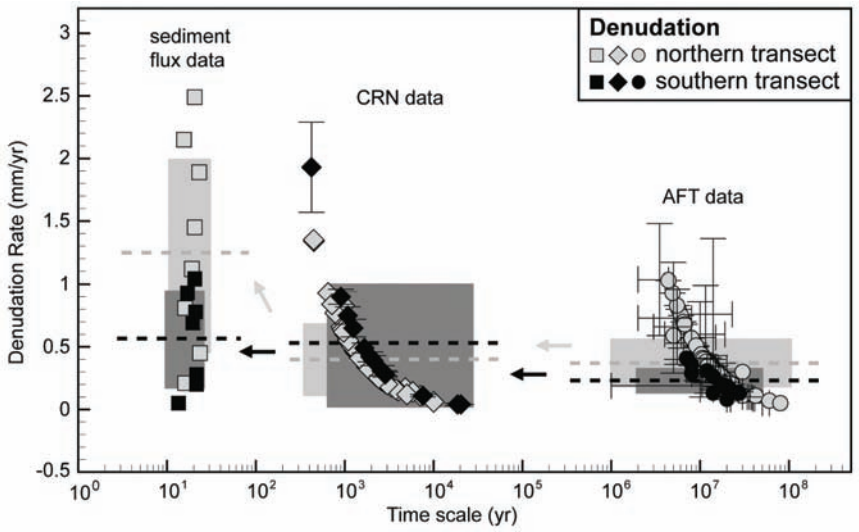

Figure 5.4: Comparison of the temporal variations in denudation rates for the northern (light gray) and southern (black) transects in Bolivia. Dashed lines indicate best estimation of mean denudation rates. Solid boxes show one sigma standard deviation of denudation rates. Arrows highlight the change in denudation over time. Circles represent values from apatite fission track data (calculated from previously published data: (Barnes et al., 2006; Gillis et al., 2006; Safran et al., 2006; Barnes et al., 2008; McQuarrie et al., 2008b) with error bars representing range of acceptable rates, diamonds show cosmogenic radionuclide-derived denudation rates (this study and from Safran et al. (2005), squares show denudation rates from sediment flux data (Barnes et al., 2006).

gauging stations for drainage basin sizes between 1600 and 59,800 km^2 (Figs. 5.2b and 5.3b) (Guyot et al., 1990; Barnes and Pelletier, 2006). Short-term denudation rates range between 0.05 mm yr^{-1} and 1.04 mm yr $^{-1}$, with a mean value of 0.57±0.39 mm yr^{-1} (Fig. 5.4). The range and mean of short-term denudation rates in the southern transect are very similar to the medium-term denudation rates (0.51±0.50 mm yr $^{-1}$, Fig. 5.4). Long-term denudation rates from AFT data range between ∼0.1-0.3 mm yr^{-1} (mean of ∼0.20±0.07 mm yr^{-1}) for the EC, 0.08-0.2 mm yr^{-1} (mean of ∼0.15±0.06 mm yr^{-1}) for the IA, and 0.2-0.4 mm yr^{-1} (mean of ∼0.31±0.11 mm yr^{-1}) or more for the SA (Figs. 5.3b and 5.4). The total long-term mean denudation rate estimated from best-fit denudation rates for the southern transect is 0.22±0.09 mm yr^{-1}, indicating that long-term denudation rates in the south are similar to medium-term denudation rates within error (Fig. 5.4). However, a

direct comparison between medium- and long-term denudation rates along the same structures in the southern SA shows a moderate increase in denudation towards the present at specific locations (e.g. S03/SA2, S11/SA3, Suppl. 5.2).

Caution should be used when comparing short- and medium-term denudation rates from Bolivia due to the limited amount of data available and the large difference in drainage basin sizes used for short timescale sediment flux determinations relative to the CRN-derived rates. For example, although the mean denudation rate in the southern transect is very similar for short- and medium-term timescales, a comparison between individual sites (e.g., S04/PZ, S06/NU, S10/SA) reveals a two to three times higher denudation rate from sediment-flux data than for CRN-derived data (Suppl. 5.2). This discrepancy in denudation rates may indeed be true for all drainage basins in this region (e.g. if the area is in topographic steady state) but a larger data set is needed from future work to verify this. Differences between short and medium-scale denudation rates are often associated with humans acting as geomorphic agents (e.g., Hooke, 2000; Wilkinson and McElroy, 2007). However, human population in the Bolivian Andes is relatively sparse and smaller villages in most mountain drainages in the Andes have been populated for millennia (Harden, 2006) with small-scale agricultural practices commencing 3.5-3.0 ka (e.g., Binford et al., 1997; Paduano et al., 2003). Most of the catchments sampled in this study were selected because they have a very low population density, minimal agricultural activity, and limited to no deforestation and therefore suggest anthropogenic effects on CRN-derived and modern denudation rates are low.

5.5.3 Denudation rates, morphology and climate

Previous studies have suggested that morphologic parameters (e.g. elevation, relief, slope, lithology, drainage size) and climate related factors (e.g. precipitation, vegetation, runoff) can have a large influence on denudation rates (e.g., Ahnert, 1970; Pinet and Souriau, 1988; Summerfield and Hulton, 1994; Pazzaglia and Brandon, 2001; Reiners et al., 2003). In this section, we explore the relationships between basin size, mean local relief, slope and elevation, mean annual precipitation, and our CRN-derived denudation rates. Comparison between morphologic and climate parameters is also conducted to investigate if the parameters are the source of the large variability detected in CRN-derived denudation rates.

Previous studies have demonstrated a negative correlation between drainage basin size and denudation that has been suggested to result from the decreasing ratio of sediment production and sediment storage (Summerfield and Hulton, 1994; Hovius, 1998). Fig. 5.5 shows denudation rate versus sample upstream drainage basin area. Results indicate that denudation rates do not correlate with catchment sizes ($r^2<0.11$). Drainage areas upstream of CRN sample locations vary largely in size and range from 4 to 10,900 km^2. High medium-term denudation rates with magnitudes exceeding 1 mm yr^{-1} and low medium-term denudation rates with values less than 0.1 mm yr^{-1} are reported for individual basins that differ in size by two orders of magnitude (Fig. 5.5). Short- term denudation rates are above 1.0 mm yr^{-1} for several basins with areas between 272 and 67,200 km^2 and less than 0.1 mm yr^{-1} for a basin with 4200 km^2 in size. These results show that denudation rates for different basins do not depend on the size of the catchment, and that there is no systematic bias in our comparison of denudation rates from basins of different size. We also find no covariance in denudation rate with basin area and other parameters (e.g.

slope or relief), and illustrate this by indicating the drainage basin size in other plots (Fig. 5.6).

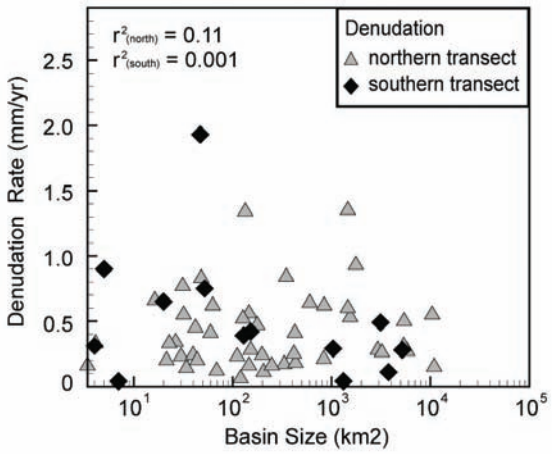

Figure 5.5: Cosmogenic radionuclide-derived denudation rates for different basin sizes. The northern transect includes 43 samples from Safran et al. (2005).

We also find no statistically significant correlation between denudation rates (CRN-derived) and local relief or slope as previously suggested (Fig. 5.6) (e.g., Ahnert, 1970; Pinet and Souriau, 1988; Summerfield and Hulton, 1994; Pazzaglia and Brandon, 2001; Schaller et al., 2001; Montgomery and Brandon, 2002). Northern transect samples including samples from Safran et al. (2005) are mostly from the high-relief region of the EC, while most of the samples from the southern transect are located in the lower-relief SA. However, both transects include samples from all the different thrust belt zones including the EC, IA, and SA and span an overall 2 km-radius relief range from 414 to 1340 m (Table 5.1). Our data indicate that CRN-derived denudation rates do not correlate with relief (r^2 <0.11, Fig. 5.6a). Denudation rates are between 0.04 and 1.93 mm yr^{-1} for samples with low relief (<750 m) and between 0.04 and 1.35 mm yr^{-1} for samples with higher relief. Slopes are steepest in the northern EC with values up to ∼56%, while the mean slope along the southern thrust belt is ∼25-30%. Our data do not show a correlation between CRN-derived

denudation rates and mean basin slope (r^2 <0.05, Fig. 5.6b). In addition, no correlation exists between CRN-derived denudation rates and sample elevation (r^2 <0.28, Fig. 5.6c). However, a moderate correlation exists between CRN-derived denudation rates and elevation, relief, and slope respectively for big basins with a drainage area >1000 km^2 in the southern transect with r^2 values between 0.7 and 0.8.

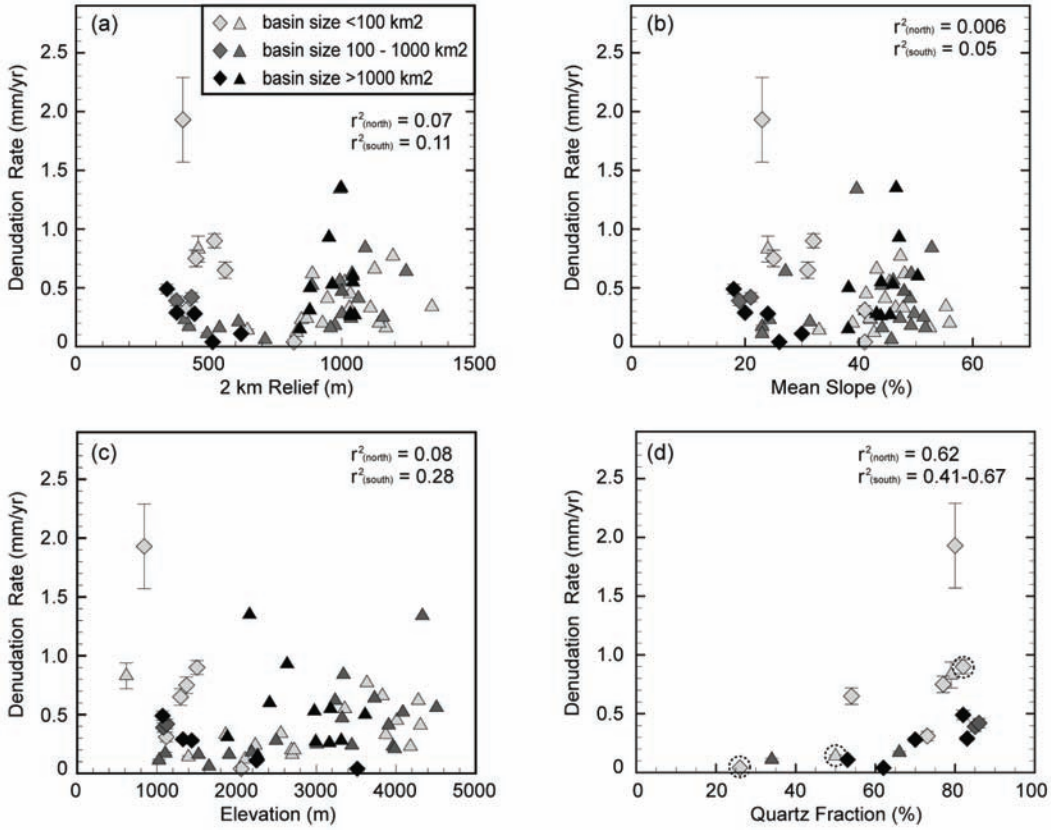

Figure 5.6: Cosmogenic radionuclide (CRN)-derived denudation rates versus geomorphologic indices resolved for basin sizes. Diamonds represent samples from the southern transect, triangles are denudation rates from the northern transect. The northern transect includes 43 denudation rates from Safran et al. (2005). (a) CRN-derived denudation rates versus relief (2 km radius). No statistical correlation exists. (b) CRN-derived denudation rates versus mean basin slope. No statistical correlation can be detected. (c) CRN-derived denudation rates versus elevation. No statistical correlation exists. (d) CRN-derived denudation rates versus quartz content. Weak positive correlation. Quartz yield represents rate of weathering, not an index for lithology. Dotted circles mark the three Devonian samples to highlight the discrepancy between quartz content and lithological age.

The impact of modern climate, and in particular precipitation, on denudation rates is still debated (e.g., Riebe et al., 2001; Burbank et al., 2003; Reiners et al.,

2003). As described above, latitudinal variations in orogen width, exhumation depth, and rock uplift rate in the central Andes have been attributed to a long- strike differences in climate and associated denudation. Fig. 5.7 shows the range of short- and medium-term denudation and precipitation rates for the northern and southern transects. The present-day climate pattern is based on an interpolation of a network of rainfall stations (Peterson and Vose, 1997). This approach has the benefit of providing calculated climate norms over a longer times scale (10 to ∼90 yr), but has the shortcoming of missing local orographic variations in climate between stations. To address the potential variability in local climate missed in the stations we compared our precipitation rates over each drainage basin to a shorter term (∼8 yr) and higher spatial resolution record determined from TRMM satellite data (Bookhagen and Strecker, 2008). In general, we find that the historical climate data capture regional spatial variations in the mean precipitation rate, and have the added advantage of providing a climate norm calculated over multiple El Niño cycles (e.g. Fig. 5.1b).

Short-term sediment flux-derived denudation rates are consistent with the modern precipitation pattern but medium-term CRN-derived rates are not. The northern transect increases in precipitation from ∼500 mm yr^{-1} in the southwest to ∼1700 mm yr^{-1} in the northeast (Figs. 5.1b and 5.7a). The southern transect is characterized by low precipitation from between 250 mm yr^{-1} in the west to ∼700 mm yr^{-1} in the east (Figs. 5.1b and 5.7b).The sediment flux-derived mean denudation rate is 2-3 times higher in the northern transect than in the southern transect, reflecting the precipitation gradient with decreasing rates from the north to the south (Fig. 5.7). However, CRN-derived mean denudation rates in the north and south are essentially the same within 1σ error (0.40 ± 0.29 mm yr^{-1} vs. 0.51 ± 0.50 mm yr^{-1}), indicating that denudation rates averaged over several thousand

years do not correlate with the present-day latitudinal climate gradient (Fig. 5.7). Moreover, basins in the northern SA,where precipitation is highest, show the same range in CRN-derived denudation magnitudes as previously estimated rates for the more arid EC (Fig. 5.7a) (Safran et al., 2005). In the southern transect, differences in mean annual precipitation between individual sample locations along the profile are too small to determine a correlation between climate and denudation.

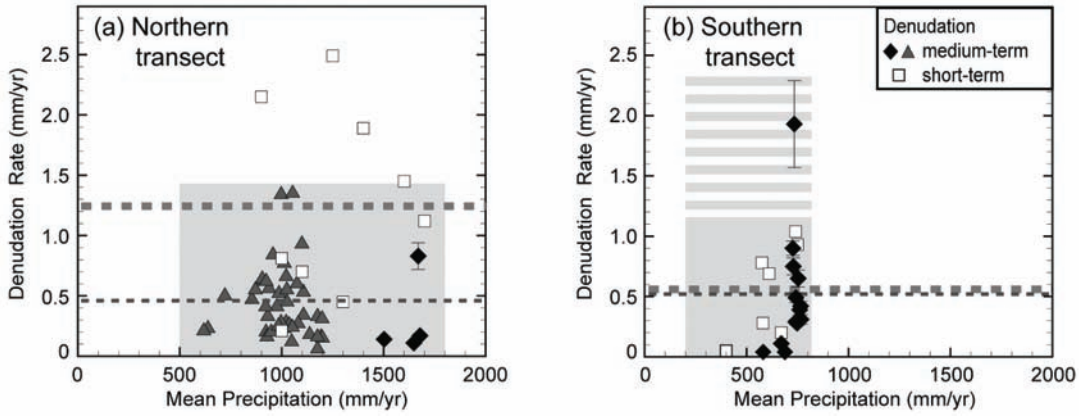

Figure 5.7: Latitudinal variations in denudation and precipitation across two transects in Bolivia. Medium-term (CRN-derived) denudation rates in the north include samples from Safran et al. (2005) (grey triangles, diamonds are from this study). Short-term (sediment flux-derived) denudation rates are from Barnes et al. (2006) (white squares). The gray box highlights the range of medium- term denudation (striped part includes the exceptionally high rate) and precipitation. The thin dashed line represents mean medium-term denudation rates (calculated for all samples in each transect), the thick dashed line represents mean short-term denudation rate. (a) Northern transect. (b) Southern transect.

The precipitation in the Bolivian Andes is highly seasonal with ∼80% of precipitation falling in austral summer (Garreaud, 2000). Previous studies have suggested that denudation is related to storm activity and extreme precipitation events rather than mean annual precipitation (e.g., Coppus and Imeson, 2002). We have compared denudation rates with maximum summer precipitation, in addition to the mean annual rainfall reported above, and come to the same conclusion; no direct relationship can be found between CRN-derived denudation rates and summer precipitation.

5.6 Discussion

Previous studies suggest several factors influence spatial and temporal variations in orogen denudation. For example, Montgomery and Brandon (2002) showed a linear relationship between denudation magnitude and mean slope for tectonically inactive regions with a mean slope $<25^{\circ}$ and either a weak linear or strong non-linear relation between denudation rate and mean slopes $>30^{\circ}$ in active tectonic settings. A correlation between climate and denudation has been found locally in areas where precipitation varies by an order of magnitude (Reiners et al., 2003). Alternatively, settings where large temporal variations in climate influence hillslope processes and vegetation (Schaller et al., 2002) have led to the interpretation that pronounced climate change might exert a larger control over denudation than the inter-regional climate variability (von Blanckenburg, 2005). Recent work by Stock et al. (2009) in the tectonically active and partially glaciated Wasatch Mountains, Utah, USA has documented large spatial and temporal variations in denudation recorded from similar geo- and thermochronology approaches as used in this study. Results from the Wasatch Mountains and the Bolivian Andes, including those presented here, do not show clear relationships between denudation, tectonics, climate, or landscape morphology thereby making it difficult to determine the factors influencing denudation rates. In the following, we discuss possible reasons for the observed spatial and temporal variations in denudation.

5.6.1 Lithologic and tectonic controls on denudation rates

The large range in calculated denudation rates (Table 5.1, Fig. 5.2) could be the result of local basin characteristics. For example, differences in lithology and the erodibility of different rock types have been suggested as a noticeable effect upon denudation rates in the Bolivian Andes (e.g., Aalto et al., 2006). Previous studies have classified the lithologies in the region into a small number of homogenous groups (igneous, meta-sedimentary, weak-sedimentary rocks) and ascribed an index representing the quartz content or the relative rates of chemical erosion to account for different rock strength (Safran et al., 2005; Aalto et al., 2006). Safran et al. (2005) corrected their CRN-derived denudation for the quartz content in different lithologies by ascribing a higher quartz fraction to areas underlain by plutons, conglomerates, and late Miocene deposits. The correction for local quartz fraction made a relatively small difference to the overall frequency distribution of denudation rates. In most of the basins characterized by a >20% difference between corrected and uncorrected estimated denudation rates the quartz-rich lithologies (i.e. plutons) occupy high terrain and the correction resulted in an increase in estimated denudation. Lithologies within our sampled catchments are composed of metasedimentary rocks and all fall into the same previously defined groups of erosive indexes, despite their differences in stratigraphic age (Table 5.1). Therefore, we assume that the underlying lithology in the study area does not have a direct effect on denudation rates. However, we estimated the quartz yield for each sample based on the quartz content derived from the sample material (e.g. the amount of quartz in relation to other minerals within the sample). The quartz yield in the analyzed grain size fraction for individual samples spans a wide range between 34% and 83%. These percentages do not reflect the quartz distribution in the source lithologies, but instead most likely indicate the

degree of weathering for different sample sites. For example, small basins exposing Devonian aged metasediments have a large variance in quartz contents of 26, 50, and 82% (Table 5.1, Fig. 5.6d). Catchments with the lowest denudation rates show low quartz content, while catchments with high denudation rates are characterized by material with high abundance of quartz (Fig. 5.6d).

High denudation rates found in some of the smaller basins (e.g. N02, S03, S11, S13, S16) may reflect active faulting along basin bounding thrusts, but in general, we find no relationship between denudation rates and structural activity of different regions. What is known is the SA are the most tectonically active part of the central Andean fold-thrust belt and characterized by broad, large wavelength synclinal basins separated by narrow zones of thrust-faulted anticlines (e.g., Baby et al., 1992; Dunn et al., 1995; Lamb, 2000). Evidence for recent deformation along previously mapped faults is not present. For example, field mapping and analysis of aerial photos at each sample location does not show recent faulting or landsliding in the sampled catchments. In addition, modern earthquakes in the region are typically moderate to deep in depth ($\sim$20 to 30 km in the north, between 50 and 600 km in the south) and associated with deeper subduction related deformation rather than near surface Holocene to Quaternary deformation (IRIS, 2009).

We might expect erosion rates to reflect the dominantly eastward propagation of SA deformation with time. Unfortunately, evidence for out-of-sequence deformation exists (e.g., Barke and Lamb, 2006; Uba et al., 2009) but is poorly constrained relative to the temporal scales over which the CRN-derived denudation rates average. Some basins (e.g. N02) are located along the frontal range and have high denudation rates perhaps reflective of active deformation whereas others (N04, N06) are located within major thrust faults but exhibit low denudation rates, possibly due

to locally reduced deformation. In the southern transect, small basins with high denudation rates (e.g. S03, S11, S13, S16: >0.65 mm yr^{-1}) lie in the hanging walls of major thrust faults in the western part of the SA, while basins located along the frontal range (e.g. S01, S08, S09) have intermediate denudation rates of ∼0.3 to 0.4 mm yr^{-1}. This pattern could be recent out-of sequence deformation that would result in the frontal-most structure not being the most active one (e.g., Barke and Lamb, 2006; Uba et al., 2009). However, other calculated denudation rates do not correlate with tectonic structures in the SA. For example, basin S05 has the lowest denudation rate (0.04 mm yr^{-1}) despite the high relief, steep slopes and a location within the hanging wall of a major thrust fault. In summary, no obvious relationship exists between CRN-derived denudation rates and fault activity.

5.6.2 Sediment transport and storage

One of the most prominent processes that might influence spatial and temporal variations in catchment denudation is mass-movements such as landslides. Landslides are an important source of sediment supply that might lead to overestimation of denudation rates derived from CRN data (e.g., Hovius et al., 2000; Gabet et al., 2004). Alternatively, modeling studies have shown that in some landslide dominated landscapes CRN-derived denudation rates can underestimate the true catchment-averaged denudation rate in small catchments (Niemi et al., 2005; Yanites et al., 2009). However, our sampled regions are not landslide dominated, and it is unlikely that the small basin S05 (∼7 km^2) that is characterized by very low denudation (0.04 mm yr^{-1}, Fig. 5.2) but high relief (∼820 m) and steep slopes (40%) can be attributed to an underestimation of denudation due to landsliding. Nevertheless, landslides are prominent features in the northern EC (e.g., Blodgett and Isacks,

2007) and we suggest that the variability in medium- and short-term denudation in these basins could be in part ascribed to mass-wasting processes.

Temporal storage of sediment within drainage basins could influence CRN abundance and therefore medium-term denudation rates (Bierman and Steig, 1996). Sediment storage within a catchment can increase the measured CRN concentration if sediments are exposed, or alternatively decrease the concentration if sediments are shielded by burial and CRN decay. More sediment storage would be expected in larger basins, but none of the big rivers in the study area show extensive floodplains within the Andes, and instead generally cut through the steep, high relief terrain. A relatively short and fast sediment cycle has been observed for large basins ($\sim 10^3$ and 10^6 km^2 drainage area) in the northern Bolivian Andes with a residence time for sediments of only $\sim$3 ka (Dosseto et al., 2006). In this study, we sampled significantly smaller catchments with lower residence times and CRN-derived denudation rates incorporating several sediment cycles. No additional CRN accumulation is observed during sediment storage so the cosmogenic denudation signal is preserved (Wittmann et al., 2009; Wittmann and von Blanckenburg, 2009).

The short-term denudation rates derived from sediment-flux data could be potentially biased by modern sediment cycle conditions. Sediment transport and deposition are highly dynamic processes that vary over time and short-term denudation rates from sediment flux data are subject to seasonal-to-decadal- scale fluctuations and the effects of transient sediment storage (e.g., Kirchner et al., 2001). Therefore, short-term denudation rates might reflect only a specific episode within the transport cycle that records a phase of high sediment flux or high sediment storage on decadal timescales. For example, a detailed study of the Pilcomayo River in southern Bolivia revealed interannual variability in river discharge related to El Niño/Southern Oscil-

lation (ENSO) with lower discharge during El Niño Years (Smolders et al., 2002).

5.6.3 Potential influence of Holocene climate change on denudation

Holocene climate and vegetation change could be an explanation for the observed temporal differences in denudation rates and the discrepancy between medium-term denudation and present-day precipitation. Terrestrial paleoclimate records indicate significant climate variations on millennial and orbital timescales affected the central Andes (Baker et al., 2001a,b; Abbott et al., 2003). Major changes in lake levels, lake sedimentation (Cross et al., 2000; Rowe et al., 2002; Abbott et al., 2003), and vegetation (Graf, 1981; Bush et al., 2005) suggest changes in both precipitation and temperature. Central Andean paleoclimate records show an overall pattern of aridity from the late Pleistocene through the MH in Bolivia (e.g., Cross et al., 2000; Baker et al., 2001b; Rowe et al., 2002; Abbott et al., 2003; Servant and Servant-Vildary, 2003).

Climate changes in the central Andes were linked to modifications in insolation due to changes in orbital parameters, ENSO, and Atlantic sea surface temperatures (e.g., Baker et al., 2001a,b; Moy et al., 2002; Servant and Servant-Vildary, 2003). ENSO is the most likely reason for precipitation changes on MH timescales and is driven by orbital fluctuations. ENSO is an important factor in the modern climate system over the Andean region with a weak tendency towards below average precipitation during El Niño summers over the Bolivian Altiplano (Vuille, 1999). Model results and observations have shown significant variations in the strength and frequency of ENSO in the past with (1) a more El Niño-like climate stage between 8 and 5 ka (Rollins et al., 1986; Sandweiss et al., 1996), (2) a steady increase in warm ENSO events over the Holocene, with a peak intensity and frequency of these events at

∼1.2 ka (Clement et al., 2000; Moy et al., 2002), and (3) a larger ENSO variability in the last 1.5 ka (Moy et al., 2002; Servant and Servant-Vildary, 2003).

The effects of ENSO variability are different in the northern and southern regions of Bolivia. In the northern Bolivian Andes, the MH dry phase (∼6 ka) was followed by large magnitude climatic change including a sharp increase in stormy type precipitation between 4.5 and 3.2 ka and an intensification of erosion in the Lake Titicaca watershed on the Altiplano between 4.5 and 2.7 ka (e.g., Abbott et al., 1997; Servant and Servant-Vildary, 2003). After 2.7 ka, coinciding with an increased frequency in El Niño, Lake Titicaca decreased and erosion weakened in the north of the Bolivian Andes, while precipitation was more uniformly distributed (Servant and Servant-Vildary, 2003). These conditions persisted until 0.5 ka, coinciding with the highest El Niño variability of the Holocene. However, convective rainfall did not reach the southern Bolivian Andes and dry conditions remain as evident from aeolian sand dunes, dated 3.5 to 2 ka, extending along the Andes between 18° and 23°S (Servant et al., 1981). The onset of modern conditions in the southern part of the Bolivian Andes was much later than in the north and took place at ∼2.3 ka (e.g., Abbott et al., 2003).

Significant differences between present-day precipitation patterns and climate conditions during the past could have an intrinsic effect on denudation in the central Andes. Denudation rates averaged over thousands of years would not reflect the distinct climate characteristics of today, but would (at least partially) possess an inherited signal from the previous climate. We quantify the potential effect of climate change on CRN-derived denudation rates (Fig. 5.8). A numerical model was used to evaluate the sensitivity of CRN-derived denudation rates to temporal variations in climate and denudation (for model details see Schaller et al. 2002; Schaller and

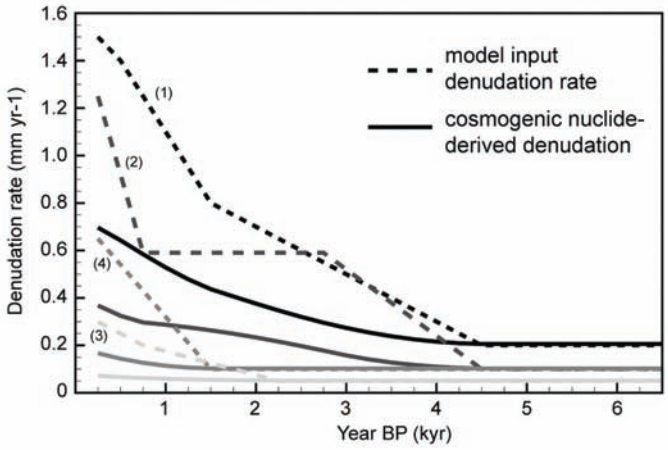

Figure 5.8: Model calculation of the sensitivity of cosmogenic radionuclide-derived denudation rates to changing climate conditions between the mid-Holocene and the present (e.g., Baker et al., 2001b; Abbott et al., 2003; Servant and Servant-Vildary, 2003). Four different scenarios are presented: (1) a steady increase in denudation rate since 4.5 ka with an input denudation rate for the arid period before 4.5 ka of 0.20 mm yr^{-1}, a constant increase in denudation to 0.80 mm yr^{-1} at 1.5 ka and a steeper increase in denudation to 1.5 mm yr^{-1} at present times (black dotted line); (2) an initial denudation rate of 0.10 mm yr^{-1} with an increase to 0.59 mm yr^{-1} between 4.5 and 2.75 ka, a period of constant denudation until 0.75 ka and a significant increase to 1.25 mm yr^{-1} at modern times (dark gray line); and (3 and 4) calculated cosmogenic nuclide denudation histories for an increase in denudation rate since 2.25 ka and 1.5 ka, respectively, with initial denudation rates of 0.05 and 0.10 mm yr^{-1} and a steady increase to 0.3 and 0.7 mm yr^{-1} at present (medium and light gray lines).

Ehlers 2006). The model uses a climate-driven input denudation history to calculate a cosmogenic ^{10}Be-derived denudation history (Schaller et al., 2001). Temporal variations in the surface and subsurface CRN concentrations for each time step are calculated by numerical integration of a depth-dependent production based on the input denudation rate from the previous step. In our simulations for the Bolivian Andes, we assume low denudation (0.05−0.2 mm yr^{-1}) rates during the MH due to the recorded aridity in Bolivia for our initial conditions. Next, we invoke an increase in denudation rates to modern values (0.30-1.5 mm yr^{-1}) in different time-step scenarios reflecting an onset of wetter conditions (Cross et al., 2000; Abbott et al., 2003). The magnitude of increase in denudation rates associated with wetter conditions in the Andes is unknown. Given this, a plausible range of increases in denudation is explored by evaluating four different scenarios for the magnitude of denudation rate

changes between 0-4.5 ka.

The model settings reflect continuous increase in denudation since 4.5 ka and 2.25 ka respectively, imitating the onset of wetter conditions in the northern and southern part of the Altiplano (Fig. 5.8, (1) and (3)). A stepwise increase in denudation since 4.5 ka, with higher denudation between 4.5 to 2.7 ka, a constant denudation until 0.5 ka, and modern increase in denudation reflects the observed precipitation and denudation pattern in the northern Andes (Fig. 5.8, (2)). A uniform increase in denudation for the last 1.5 ka is related to the high ENSO variability during that time interval (Fig. 5.8, (4)). Calculated modern CRN-derived denudation rates at the end of each simulation vary between 0.07 and 0.7 mm yr^{-1} and are in good agreement with our observations. The simulations indicate that changes in precipitation lead to a slow adjustment of the CRN concentration, but that it can take thousands of years before the CRNs are in complete equilibrium with the new climate (or denudation) conditions as previously noted (Schaller et al., 2001; Niemi et al., 2005; Schaller and Ehlers, 2006). This conclusion is consistent with a recent study that ascribed fluctuations between high and low denudation periods to changes in climate over medium-term timescales (Dosseto et al., 2006).

In summary, the 3-fold discrepancy between short- and medium- term denudation rates in northern Bolivia can be reconciled if the following conditions are met: (a) aridity in the MH causing very low (<0.1 mm yr^{-1}) denudation rates, (b) an onset of wetter conditions between 4.5 and 1.5 ka was accompanied by increasing denudation rates, and (c) overall changes in denudation rates are large over medium-term timescales.

5.7 Implications and Conclusions

Our results exhibit large spatial and temporal variations in denudation rates across the central Andes in Bolivia. Cosmogenic ^{10}Be concentrations from modern river sediments indicate catchment-averaged denudation rates of 0.04− 1.93 mm yr^{-1} with apparent ages of 0.4 to 20 ka. No statistically significant correlation exists between CRN-derived denudation rates and morphological indices such as relief, slope or basin size. However, smaller basins reflect a much higher variability in denudation rates, probably due to local basin parameters (e.g. proximity to active faults,). Latitudinal variations in precipitation are not reflected in the CRN-derived denudation rates.

Denudation rates averaged over long- ($>10^6$ yrs) and medium-term (10^2 -10^4 yrs) timescales are similar and within error of each other. Consistency between CRN-derived denudation rates and the much longer-term fission-track exhumation rates implies that on average denudation rates over the last several millions years in the central Andes might have been similar. However, a comparison between best-fit denudation rates estimated from AFT data and CRN-derived data from similar locations along the southern transect suggest at the 1σ-level a moderate increase in denudation rates over time. The along-strike contrast in denudation might have existed since the Miocene, but the total magnitude is difficult to constrain due to large errors associated with the long-term denudation magnitudes. A significant increase in denudation rates over the last several thousand years is observed with sediment flux-derived denudation rates $\sim$3 times higher than CRN- derived denudation rates in the northern transect. Our data, which cover a previously sparsely sampled medium-term timescale, indicate that the increase in short-term (10^1 yrs) denudation rates is relatively recent and that it might be associated with an increase

in precipitation since ∼4.5 ka. Climate model simulations of the study area indicate that the Bolivian Andes likely experienced a general increase in precipitation since the mid-Holocene. Climate shifts towards more humid conditions and/or towards more variable conditions in the Bolivian Andes may have had a substantial influence on denudation rates.

In summary, our results suggest that the effect of an increase in Holocene precipitation rates over the last ∼4.5 ka on denudation rates is prevalent in the CRN data. Thus, CRN data from the central Andes may not reflect the modern climate. Other factors that might have contributed to the recent increase in denudation rates are an increase in sediment yield and/or the sensitivity of sediment flux data to episodic changes in denudation or storage that may influence such data over short time scales.

5.8 Acknowledgments

We thank SERGIOTECMIN of La Paz, Bolivia, and Jaime Tito for logistical support. Financial support was provided to T. Ehlers and C. Poulsen by the US National Science Foundation (EAR 0738822 and 0544954), two University of Michigan Scott Turner Awards in Earth Sciences to N. Insel, and a University of Michigan Sokol International Summer Research Fellowship in the Sciences to J. Barnes. We thank two anonymous reviewers for their insightful comments that greatly improved the manuscript.

5.9 Appendix: Supplementary Material

Supplement 5.1: Apatite fission track data and estimated denudation rates

Sample ID	Latitude (°S)	Longitude (°W)	Elevation (m)	pooled age (Ma)	most recent cooling Temperature (°C)[1]	most recent cooling Time (Ma)[2]	denudation rate from pooled age (mm yr^{-1})	denudation rate from cooling history (mm yr^{-1})[3]	Reference
Northern transect - Eastern Cordillera (RJ, C, T, Z, EC), Interandean Zone (IA), Subandes (SA)									
RJG7	15.91	68.23	3042	8.6	110	8.5	**0.53**	0.53	Gillis et al. 2007
RJG8	15.92	68.24	3343	10.5	110	10.9	**0.43**	0.42	Gillis et al. 2007
RJG9	15.93	68.24	3414	10.0	110	10.1	**0.45**	0.45	Gillis et al. 2007
RJG1	15.95	68.25	3805	16.2	110	16.4	**0.28**	0.28	Gillis et al. 2007
03RJG15	15.97	68.27	3976	15.4	110	14.5	**0.30**	0.31	Gillis et al. 2007
RJG2	15.97	68.28	4074	10.3	110	10.3	**0.44**	0.44	Gillis et al. 2007
RJG3	15.99	68.29	4335	17.9	110	18.0	**0.25**	0.25	Gillis et al. 2007
03RJG16	16.03	68.30	4612	14.3	110	13.2	**0.32**	0.34	Gillis et al. 2007
RJG4	16.03	68.29	4714	10.4	110	11.9	**0.44**	0.38	Gillis et al. 2007
RJG5	16.06	68.30	5020	11.2			**0.41**		Gillis et al. 2007
RJG6	16.07	68.30	5363	18.2	110	18.2	**0.25**	0.25	Gillis et al. 2007
RZG19	16.28	68.14	5400	16.3			**0.28**		Gillis et al. 2007
C1B	16.08	68.24	4640	20.0			**0.23**		Safran et al. 2006
C1C	16.08	68.24	4630	19.1			**0.24**		Safran et al. 2006
C2	16.00	68.17	2875	9.1			**0.50**		Safran et al. 2006
C4	15.99	68.17	3070	10.7			**0.42**		Safran et al. 2006
C5	15.99	68.18	3380	10.9			**0.42**		Safran et al. 2006
C7	15.99	68.24	4115	19.2			**0.24**		Safran et al. 2006
C8	16.01	68.25	4388	23.0			**0.20**		Safran et al. 2006
C9	16.03	68.26	4580	17.9			**0.25**		Safran et al. 2006
C10A	16.05	68.29	4800	12.5			**0.36**		Safran et al. 2006
C10B	16.05	68.29	4800	17.6			**0.26**		Safran et al. 2006
C11	16.06	68.30	5020	14.7			**0.31**		Safran et al. 2006
T1	16.49	67.89	4640	5.7			**0.80**		Safran et al. 2006
T2	16.49	67.88	4490	6.1			**0.75**		Safran et al. 2006
T4	16.48	67.86	4080	6.5			**0.70**		Safran et al. 2006
T5	16.47	67.85	3800	8.0			**0.57**		Safran et al. 2006
T6	16.46	67.83	3500	5.5			**0.83**		Safran et al. 2006
T7	16.44	67.82	3240	10.5			**0.43**		Safran et al. 2006
Z-3	16.10	68.07	2040	6.7			**0.68**		Benjamin et al. 1987
Z-4	16.12	68.09	2380	11.4			**0.40**		Benjamin et al. 1987
Z-5	16.13	68.11	2680	8.0			**0.57**		Benjamin et al. 1987
Z-6	16.15	68.12	3000	14.1			**0.32**		Benjamin et al. 1987
Z-7	16.16	68.13	3300	4.9			**0.93**		Benjamin et al. 1987
Z-9	16.17	68.14	3450	9.0			**0.51**		Benjamin et al. 1987
Z-10	16.24	68.12	4280	10.3			**0.44**		Benjamin et al. 1987
Z-11	16.27	68.12	4560	15.5			**0.29**		Benjamin et al. 1987
Z-12	16.29	68.13	4780	11.7			**0.39**		Benjamin et al. 1987
EC0-1	16.96	67.80	2529	4.4			1.03		McQuarrie et al. 2008a
EC2-1	16.88	67.72	2148	49.8	75	2-5	0.09	**0.59** - 1.48	McQuarrie et al. 2008a
EC2-2	16.34	68.04	4572	8.3	110	11-14	0.55	0.32 - **0.41**	McQuarrie et al. 2008a
EC3	16.33	67.97	3770	85.8	100	3-25	0.05	**0.16** - 1.36	Barnes et al. 2006
EC3-1	16.31	67.91	3246	12.6	140	16-20	**0.36**	0.30 - 0.37	McQuarrie et al. 2008a
EC3-2	16.25	67.79	2286	42.1	85	30-50	**0.11**	0.07 - 0.11	McQuarrie et al. 2008a
IA1-1	15.83	67.53	1160	30.3	90	30-38	0.14	0.09 - **0.11**	McQuarrie et al. 2008a
IA1-2	15.82	67.51	875	60	85	30-50	**0.07**	0.06 - 0.11	McQuarrie et al. 2008a
IA3	15.78	67.50	600	14	100	9-20	**0.31**	0.19 - 0.43	Barnes et al. 2006
IA3-1	15.78	67.51	1023	13.2	130	14-15	**0.33**	0.29 - 0.37	McQuarrie et al. 2008a
IA3-2	15.83	67.42	1680	79.9	80	>55	**0.05**	∼0.05	McQuarrie et al. 2008a
IA4	15.77	67.49	760	10.5		5-15	**0.41**	0.29 - 0.86	Barnes et al. 2006
IA5	15.72	67.50	1160	10.9		5-15	**0.40**	0.29 - 0.86	Barnes et al. 2006
IA6	15.70	67.50	1480	11.5		5-15	**0.38**	0.29 - 0.86	Barnes et al. 2006
IA8	15.68	67.49	1400	12.3		5-15	**0.35**	0.29 - 0.86	Barnes et al. 2006
SA1	15.6	67.44	522	116	90	11-30	0.03	**0.10** - 0.28	Barnes et al. 2006
SA3	15.4	67.14	820	6.62		4-19	0.60	**0.21** - 0.99	Barnes et al. 2006
SA4	15.37	67.11	640	51.5		4-19	0.08	**0.21** - 0.99	Barnes et al. 2006
SA5	15.23	67.07	790	91.4		4-19	0.04	**0.21** - 0.99	Barnes et al. 2006

Supplement 5.1 (continue): Apatite fission track data and estimated denudation rates

Sample ID	Latitude (°S)	Longitude (°W)	Elevation (m)	pooled age (Ma)	most recent cooling Temperature (°C)[1]	most recent cooling Time (Ma)[2]	denudation rate from pooled age (mm yr^{-1})	denudation rate from cooling history (mm yr^{-1})[3]	Reference
Southern transect - Eastern Cordillera (RJ, C, T, Z, EC), Interandean Zone (IA), Subandes (SA)									
EC1	20.09	66.39	3668	30.3	60	10-14	0.12	**0.13** - 0.19	Barnes et al. 2008
EC2	19.94	66.29	3900	11.9	120	~12	**0.31**	~0.34	Barnes et al. 2008
EC3	19.95	66.25	3350	14.2	105	10-15	**0.26**	0.23 - 0.35	Barnes et al. 2008
EC5	20.04	66.17	3290	19.9	105	20-25	**0.19**	0.14 - 0.18	Barnes et al. 2008
EC6	20.00	66.17	3311	27.6	105	34-36	**0.13**	0.10 - 0.10	Barnes et al. 2008
EC7	19.86	66.14	3747	13.8	105	10-20	**0.27**	0.18 - 0.35	Barnes et al. 2008
EC10	19.58	65.27	3222	19.0	100	19-22	**0.19**	0.15 - 0.18	Barnes et al. 2008
EC11	19.34	66.16	2255	26.9	125	27-30	**0.14**	0.14 - 0.16	Barnes et al. 2008
IA1	19.08	64.82	2670	88	60	20-22	0.04	**0.08** - 0.08	Barnes et al. 2008
IA2	19.06	64.77	2371	19.4	100	20-22	0.18	0.14 - **0.16**	Barnes et al. 2008
IA3	19.18	64.47	2051	17.8	90	19-21	**0.20**	0.13 - 0.15	Barnes et al. 2008
SA2	19.80	64.02	1236	41.9	80	8-20	0.12	**0.16** - 0.40	Barnes et al. 2008
SA3	19.85	63.73	1367	264.3	75	3-8	0.02	**0.36** - 0.96	Barnes et al. 2008
SA4	19.81	63.72	1260	117	75	7-13	0.04	**0.22** - 0.41	Barnes et al. 2008
SA6	19.78	63.25	844	246.7	65	2-8	0.02	**0.29** - 1.17	Barnes et al. 2008

bold values: best estimates for long-term denudation rates.
[1] maximum temperature the sample was at when it began to rapidly cool.
[2] time range from which recent cooling began as constrained by best-fit thermal modeling.
[3] minimum and maximum denudation rates based on time range of the onset of recent cooling.

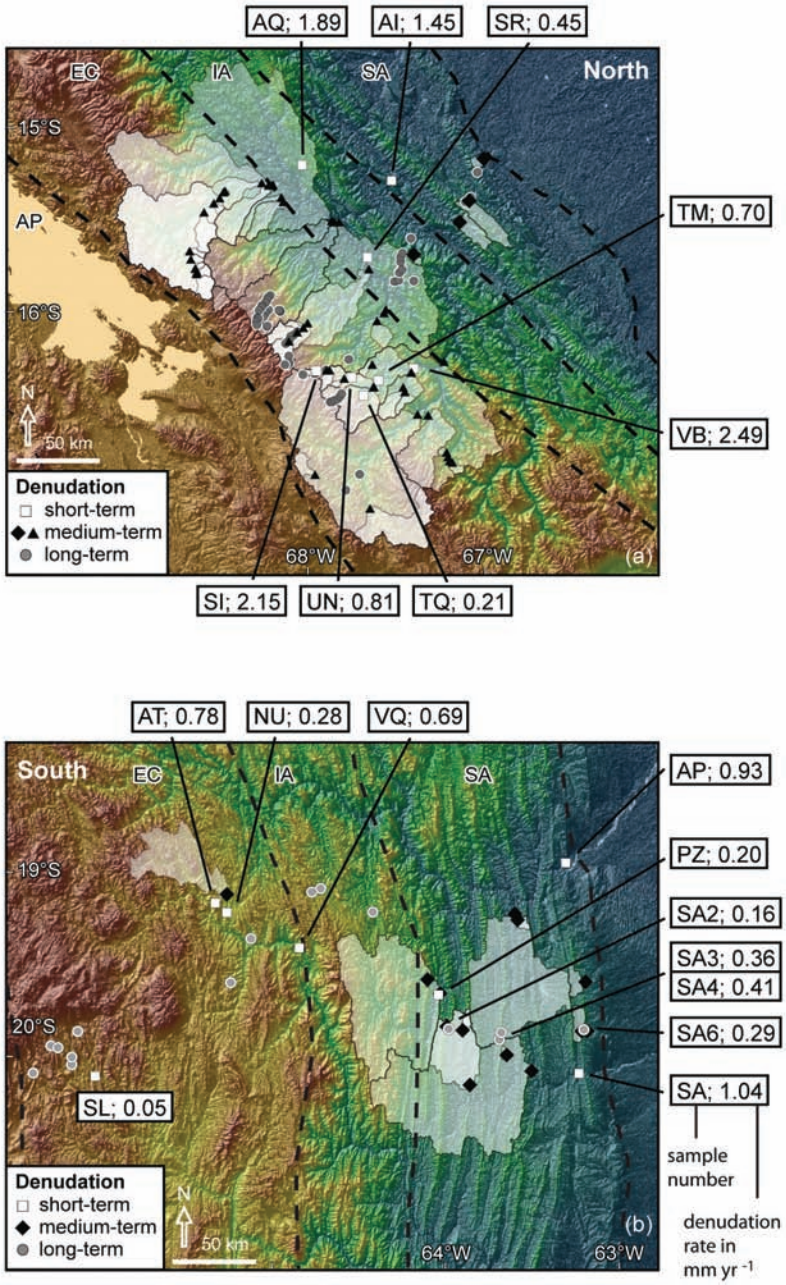

.

Supplement 5.2: Short-term denudation rates are calculated from sediment gauging stations (Barnes et al., 2006); long-term denudation calculated from previously published apatite fission track data (Barnes et al., 2008). (a) Northern transect. (b) Southern transect.

Bibliography

Aalto, R., Dunne, T. and Guyot, J. L. Geomorphic controls on Andean denudation rates. *Journal of Geology*, 114(1):85–99, 2006.

Abbott, M. B., Binford, M. W., Brenner, M. and Kelts, K. R. A 3500 14C yr High-Resolution Record of Water-Level Changes in Lake Titicaca, Bolivia/Peru. *Quaternary Research*, 47:169–180, 1997.

Abbott, M. B., Wolfe, B. B., Wolfe, A. P., Seltzer, G. O., Aravena, R., Mark, B. G., Polissar, P. J., Rodbell, D. T., Rowe, H. D. and Vuille, M. Holocene paleohydrology and glacial history of the central Andes using multiproxy lake sediment studies. *Palaeogeography, Palaeoclimatology, Palaeoecology*, 194:123–138, 2003.

Aceituno, P. On the Functioning of the Southern Oscillation in the South American Sector. Part I: Surface Climate. *Monthly Weather Review*, 116:505 – 524, 1988.

Ahnert, F. Functional relationships between denudation, relief, and uplift in large, mid-latitude drainage basins. *American Journal of Science*, 268(3):243–263, 1970.

Allmendinger, R. W., Jordan, T. E., Kay, S. M. and Isacks, B. L. The evolution of the Altiplano-Puna Plateau of the Central Andes. *Annual Review of Earth and Planetary Sciences*, 25:139–174, 1997.

Anders, M. H., Gregory-Wodzicki, K. M. and Spiegelman, M. A critical evaluation of late Tertiary accelerated uplift rates for the Eastern Cordillera, central Andes of Bolivia. *Journal of Geology*, 110(1):89–100, 2002.

Baby, P., Herail, G., Salinas, R. and Sempere, T. Geometry and kinematic evolution of passive roof duplexes deduced from cross section balancing; example from the foreland thrust system of the southern Bolivian subandean zone. *Tectonics*, 11(3):523–536, 1992.

Baker, P. A., Rigsby, C. A., Seltzer, G. O., Fritz, S. C., Lowenstein, T. K., Bacher, N. P. and Veliz, C. Tropical climate changes at millennial and orbital timescales on the Bolivian Altiplano. *Nature*, 409:698–701, 2001a.

Baker, P. A., Seltzer, G. O., Fritz, S. C., Dunbar, R. B., Grove, M. J., Tapia, P. M., Cross, S. L., Rowe, H. D. and Broda, J. P. The history of South American tropical precipitation for the past 25,000 years. *Science*, 29:640–643, 2001b.

Balco, G. Topographic shielding and cosmogenic nuclide production rates over large areas. *http://depts.washington.edu/cosmolab/math.html*, 2001.

Barke, R. and Lamb, S. Late Cenozoic uplift of the Eastern Cordillera, Bolivian Andes. *Earth and Planetary Science Letters*, 249:350–367, 2006.

Barnes, J. B. and Ehlers, T. End member models for Andean Plateau uplift. *Earth Science Reviews*, 97(1-4):105–132, 2009.

Barnes, J. B., Ehlers, T. A., McQuarrie, N., O'Sullivan, P. B. and Pelletier, J. D. Variations in Eocene to recent erosion across the central Andean fold-thrust belt, northern Bolivia: Implications for plateau evolution. *Earth and Planetary Science Letters*, 248:118–133, 2006.

Barnes, J. B., Ehlers, T. A., McQuarrie, N., O'Sullivan, P. B. and Tawackoli, S. Thermochronometer record of central Andean plateau growth, Bolivia (19.5S). *Tectonics*, 27(TC3003):doi:10.1029/2007TC002174, 2008.

Barnes, J. B. and Pelletier, J. D. Latitudinal variation of denudation in the evolution of the Bolivian Andes. *American Journal of Science*, 306:1–31, 2006.

Beaumont, C., Jamieson, R. A., Nguyen, M. H. and Lee, B. Himalayan tectonics explained by extrusion of a low-viscosity crustal channel coupled to focused surface denudation. *Nature*, 414(6865):738–742, 2001.

Benjamin, M. T., Johnson, N. M. and Naeser, C. W. Recent rapid uplift in the Bolivian Andes; evidence from fission-track dating. *Geology*, 15(7):680–683, 1987.

Bierman, P. and Steig, E. J. Estimating rates of denudation using cosmogenic isotope abundances in sediment. *Earth Surface Processes and Landforms*, 21:125–139, 1996.

Binford, M. W., Kolata, A. L., Brenner, M., Janusek, J. W., Seddon, M. T., Abbott, M. and Curtis, J. H. Climate variation and the rise and fall of an Andean civilization. *Quaternary Research*, 47(2):235–248, 1997.

Blodgett, T. A. and Isacks, B. L. Landslide erosion rate in the eastern Cordillera of Northern Bolivia. *Earth Interactions*, 11(19):1 – 30, 2007.

Bookhagen, B. and Strecker, M. R. Orographic barriers, high-resolution TRMM rainfall, and relief variations along the eastern Andes. *Geophysical Research Letters*, 35(L06403):doi:10.1029/2007GL032011, 2008.

Burbank, D. W., Blythe, A. E., Putkonen, J., Pratt-Sitaula, B., Gabet, E., Oskin, M., Barros, A. and Ojha, T. P. Decoupling of erosion and precipitation in the Himalayas. *Nature*, 426(6967):652–655, 2003.

Bush, M. B., Hansen, B. C. S., Rodbell, D. T., Seltzer, G. O., Young, K. R., Leon, B., Abbott, M. B., Silman, M. R. and Gosling, W. D. A 17 000-year history of Andean climate and vegetation change from Laguna de Chochos, Peru. *Journal of Quaternary Science*, 20:703–714, 2005.

Clement, A. C., Seager, R. and Cane, M. A. Suppression of El Nino during the mid-Holocene by changes in the Earth's orbit. *Paleoceanography*, 15(6):731 – 737, 2000.

Coppus, R. and Imeson, A. C. Extreme events controlling erosion and sediment transport in a semi-arid sub-Andean valley . *Earth Surface Processes and Landforms*, 27:1365 – 1375, 2002.

Cross, S. L., Baker, P. A., Seltzer, G. O., Fritz, S. C. and Dunbar, R. B. A new estimate of the Holocene lowstand level of Lake Titicaca, central Andes, and implications for tropical palaeohydrology. *The Holocene*, 10:21–32, 2000.

Dosseto, A., Bourdon, B., Gaillardet, J., Maurice-Bourgoin, L. and Allegre, C. J. Weathering and transport of sediments in the Bolivian Andes; time constraints from uranium-series isotopes. *Earth and Planetary Science Letters*, 248(3-4):759–771, 2006.

Dunn, J., Hartshorn, K. and Hartshorn, P. Structural styles and hydrocarbon potential of the sub-Andean thrust belt of southern Bolivia. *AAPG Memoir*, 62:523–543, 1995.

Ege, H., Sobel, E. R., Scheuber, E. and Jacobshagen, V. Exhumation history of the southern Altiplano plateau (southern Bolivia) constrained by apatite fission-track thermochronology. *Tectonics*, 26:TC1004, doi:10.1029/2005TC001869, 2007.

Ehlers, T. and Poulsen, C. J. Influence of Andean uplift on climate and paleoaltimetry estimates. *Earth and Planetary Science Letter*, 281:238–248, 2009.

Ehlers, T. A., Chaudhri, T., Kumar, S., Fuller, C. W., Willett, S. D., Ketcham, R. A., Brandon, M. T., Belton, D. X., Kohn, B. P., Gleadow, A. J., Dunai, T. J. and Fu, F. Q. Computational tools for low-temperature thermochronometer Interpretation. In Reiners, P. W. and Ehlers, T. A., editors, *Low-Temperature Thermochronology: Techniques, Interpretations, and Applications*, volume 58 of *Reviews in Mineralogy and Geochemistry*, pages 589–622. Mineralogical Society of America, Chantilly, VA, 2005.

Gabet, E. J., Burbank, D. W., Putkonen, J. K., Pratt-Sitaula, B. A. and Ojha, T. Rainfall thresholds for landsliding in the Himalayas of Nepal. *Geomorphology*, 63(3-4):131–143, 2004.

Garreaud, R. D. Intraseasonal variability of moisture and rainfall over the South American Altiplano. *Monthly Weather Review*, 128:3337 – 3346, 2000.

Garreaud, R. D. and Wallace, J. M. The diurnal march of convective cloudiness over the Americas. *Monthly Weather Review*, 125:3157 – 3171, 1997.

Garzione, C. N., Molnar, P., Libarkin, J. and MacFadden, B. Rapid late Miocene rise of the Bolivian Altiplano: Evidence for removal of mantle lithosphere. *Earth and Planetary Science Letters*, 241:543–556, 2006.

Gillis, R. J., Horton, B. K. and Grove, M. Thermochronology, geochronology, and upper crustal structure of the Cordillera Real: Implications for Cenozoic exhumation of the central Andean Plateau. *Tectonics*, 25(TC6007):doi:10.1029/2005TC001887, 2006.

Graf, K. Palynological investigations of two post-glacial peat bogs near the boundary of Bolivia and Peru. *Journal of Biogeography*, 8(5):353–368, 1981.

Guyot, J. L., Bourges, J., Hoorelbecke, R., Roche, M. A., Calle, H., Cortes, J. and Guzman, M. C. B. Suspended material discharge from the Andes to the Amazonia along the Beni River, Bolivia. In Bordas, M. P. and Walling, D. E., editors, *Sediment Budgets*, volume 174, pages 443–451. IAHS Publication 174, 1988.

Guyot, J. L., Calle, H., Cortes, J. and Pereira, M. Transport of suspended sediment and dissolved material from the Andes to the Rio de la Plata by the Bolivian tributaries of the Rio Paraguay (Rios Pilcomayo and Bermejo). *Hydrologic Sciences Journal*, 35:653–665, 1990.

Harden, C. P. Human impacts on headwater fluvial systems in the Northern and Central Andes. In James, L. A. and Marcus, W. A., editors, *Geomorphology*, volume 79, pages 249–263. 2006.

Heisinger, B., Lal, D., Jull, A. J. T., Kubik, P., Ivy-Ochs, S., Knie, K. and Nolte, E. Production of selected cosmogenic radionuclides by muons; 2, Capture of negative muons. *Earth and Planetary Science Letters*, 200(3-4):357–369, 2002.

Hilley, G. E. and Strecker, M. R. Steady state erosion of critical Coulomb wedges with applications to Taiwan and the Himalaya. *Journal of Geophysical Research*, 109:doi:10.1029/2002JB002284, 2004.

Hooke, R. L. On the history of humans as geomorphic agents. *Geology*, 28(9):843 – 846, 2000.

Horton, B. K. Sediment accumulation on top of the Andean orogenic wedge; Oligocene to late Miocene basins of the Eastern Cordillera, southern Bolivia. *Geological Society of America Bulletin*, 110(9):1174–1192, 1998.

Horton, B. K. Erosional control on the geometry and kinematics of thrust belt development in the central Andes. *Tectonics*, 18(6):1292–1304, 1999.

Hovius, N. Controls on sediment supply by large rivers. *Special Publication - SEPM (Society for Sedimentary Geology)*, 59:3–16, 1998.

Hovius, N., Stark, C. P., Chu, H.-T. and Lin, J.-C. Supply and removal of sediment in a landslide-dominated mountain belt; Central Range, Taiwan. *Journal of Geology*, 108(1):73–89, 2000.

Insel, N., Poulsen, C. J. and Ehlers, T. A. Influence of the Andes mountains on South American moisture transport, convection, and precipitation. *Climate Dynamics*, pages doi:10.1007/s00382–009–0637–1, 2009.

Isacks, B. L. Uplift of the Central Andean Plateau and bending of the Bolivian Orocline. *Journal of Geophysical Research*, 93(4):3211–3231, 1988.

Jordan, T. E., Reynolds, James H., I. and Erikson, J. P. Variability in age of initial shortening and uplift in the Central Andes. In Ruddiman, W. F., editor, *Tectonic uplift and climate change*, pages 41–61. Plenum Press, New York, 1997.

Kirchner, J. W., Finkel, R. C., Riebe, C. S., Granger, D. E., Clayton, J. L., King, J. G. and Megahan, W. F. Mountain erosion over 10 yr, 10 k.y., and 10 m.y. time scales. *Geology*, 29(7):591–594, 2001.

Kley, J. Transition from basement-involved to thin-skinned thrusting in the Cordillera Oriental of southern Bolivia. *Tectonics*, 15(4):763–775, 1996.

Kley, J. and Monaldi, C. R. Tectonic shortening and crustal thickness in the Central Andes; how good is the correlation? *Geology*, 26(8):723–726, 1998.

Lamb, S. Active deformation in the Bolivian Andes, South America. *Journal of Geophysical Research, B, Solid Earth and Planets*, 105(11):25,627–25,653, 2000.

Lenters, J. D. and Cook, K. H. Simulation and diagnosis of the regional summertime precipitation climatology of South America. *Journal of Climate*, 8(12):2988–3005, 1995.

Leturmy, P., Mugnier, J. L., Vinour, P., Baby, P., Colletta, B. and Chabron, E. Piggyback basin development above a thin-skinned thrust belt with two detachment levels as a function of interactions between tectonic and superficial mass transfer; the case of the Subandean Zone (Bolivia). *Tectonophysics*, 320(1):45–67, 2000.

Masek, J. G., Isacks, B. L., Gubbels, T. L. and Fielding, E. J. Erosion and tectonics at the margins of continental plateaus. *Journal of Geophysical Research*, 99(7):13,941–13,956, 1994.

McQuarrie, N. Initial plate geometry, shortening variations, and evolution of the Bolivian Orocline. *Geology*, 30(10):867–870, 2002.

McQuarrie, N., Barnes, J. B. and Ehlers, T. A. Geometric, kinematic,and erosional history of the central Andean Plateau, Bolivia (15-17). *Tectonics*, 27(TC3007):doi:10.1029/2006TC002054, 2008a.

McQuarrie, N., Ehlers, T. A., Barnes, J. B. and Meade, B. J. Temporal variation in climate and tectonic coupling in the central Andes. *Geology*, 36(12):999–1002, 2008b.

Montgomery, D. R., Balco, G. and Willett, S. D. Climate, tectonics, and the morphology of the Andes. *Geology*, 29(7):579–582, 2001.

Montgomery, D. R. and Brandon, M. T. Topographic controls on erosion rates in tectonically active mountain ranges. *Earth and Planetary Science Letters*, 201(3-4):481–489, 2002.

Moy, C. M., Seltzer, G. O., Rodbell, D. T. and Anderson, D. M. Variability of El Nino/southern Oscillation activity at millenial timescales during the Holocene epoch. *Nature*, 420:162 – 165, 2002.

Mulch, A., Uba, C., Strecker, M. R., Schoenberg, R. and Chamberlain, C. P. Late Miocene climate variability and surface elevation in the central Andes. *Earth and Planetary Science Letter*, 290:173 – 182, 2010.

Niemi, N. A., Oskin, M., Burbank, D. W., Heimsath, A. M. and Gabet, E. J. Effects of bedrock landslides on cosmogenically determined erosion rates. *Earth and Planetary Science Letters*, 237(3-4):480–498, 2005.

Nishiizumi, K., Imamura, M., Caffee, M. W., Southon, J. R., Finkel, R. C. and McAninch, J. Absolute calibration of 10Be AMS standards. *Nuclear Instruments and Methods in Physics Research*, B258:403–413, 2007.

Oncken, O., Hindle, D., Kley, J., Elger, K., Victor, P. and Schemmann, K. Deformation of the central Andean upper plate system - facts, fiction, and constraints for plateau models. In Oncken, O., Chong, G., Franz, G., Giese, P., Gotze, H.-J., Ramos, V. A., Strecker, M. R. and Wigger, P., editors, *The Andes: Active Subduction Orogeny*, volume 1 of *Frontiers in Earth Sciences*, pages 3–27. Springer-Verlag, Berlin, 2006.

Paduano, G. M., Bush, M. B., Baker, P. A., Fritz, S. C. and Seltzer, G. O. A vegetation and fire history of Lake Titicaca since the last glacial maximum. In Seltzer, G. O., Rodbell, D. T. and Wright, H. E., editors, *Palaeogeography, Palaeoclimatology, Palaeoecology*, volume 194, pages 259–279. 2003.

Pazzaglia, F. J. and Brandon, M. T. A fluvial record of long-term steady-state uplift and erosion across the Cascadia forearc high, western Washington State. *American Journal of Science*, 301(4-5):385–431, 2001.

Peterson, T. C. and Vose, R. S. An Overview of the Global Historical Climatology Network Temperature Base. *Bulletin of the American Meteorological Society*, 78:2837 – 2849, 1997.

Pinet, P. and Souriau, M. Continental erosion and large-scale relief. *Tectonics*, 7(3):563–582, 1988.

Reiners, P. W., Ehlers, T. A., Mitchell, S. G. and Montgomery, D. R. Coupled spatial variations in precipitation and long-term erosion rates across the Washington Cascades. *Nature*, 426:645–647, 2003.

Riebe, C., Kirchner, J., Granger, D. and Finkel, R. Strong tectonic and weak climatic control of long-term chemical weathering rates. *Geology*, 29(6):511–514, 2001.

Rollins, H. B., Richardson III, J. B. and Sandweiss, D. H. The birth of El Nino: geoarchaeological evidence and implications. *Geoarchaeology*, 1(1):3–15, 1986.

Rowe, H. D., Dunbar, R. B., Mucciarone, D. A., Seltzer, G. O., Baker, P. A. and Fritz, S. Insolation, moisture balance and climate change on the South American Altiplano since the last glacial maximum. *Climatic Change*, 52(1-2):175–199, 2002.

Safran, E. B., Bierman, P. R., Aalto, R., Dunne, T., Whipple, K. X. and Caffee, M. W. Erosion rates driven by channel network incision in the Bolivian Andes. In Heimsath, A. M. and Ehlers, T. A., editors, *Earth Surface Processes and Landforms*, volume 30, pages 1007–1024. 2005.

Safran, E. B., Blythe, A. and Thomas, D. Spatially variable exhumation rates in orogenic belts: An Andean example. *Journal fo Geology*, 114:665–681, 2006.

Sandweiss, D. H., Richardson III, J. B., Reitz, E. J., Rollins, H. B. and Maasch, K. Geoarchaelogical Evidence from Peru for a 5000 Years B.P. Onset of El Nino. *Science*, 273:1531 – 1533, 1996.

Schaller, M. and Ehlers, T. Limits to quantifying climate driven changes in denudation rates with cosmogenic radionuclides. *Earth and Planetary Science Letters*, 248:138–152, 2006.

Schaller, M., von Blanckenburg, F., Hovius, N. and Kubik, P. W. Large-scale erosion rates from in situ-produced cosmogenic nuclides in European river sediments. *Earth and Planetary Science Letters*, 188(3-4):441–458, 2001.

Schaller, M., von Blanckenburg, F., Veldkamp, A., Tebbens, L. A., Hovius, N. and Kubik, P. W. A 30 000 yr record of erosion rates from cosmogenic (super 10) Be in middle European river terraces. *Earth and Planetary Science Letters*, 204(1-2):307–320, 2002.

Sempere, T. Phanerozoic evolution of Bolivia and adjacent regions. *in Tankard, A.J. etal., eds., Petroleum basins of South America: American Association of Petreleum Geologists Memoir*, 62:511–522, 1995.

Sempere, T., Butler, R., Richards, D., Marshall, L., Sharp, W. and Swisher, C. Stratigraphy and chronology of Upper Cretaceous-lower Paleogene strata in Bolivia and Northwest Argentina. *GSA Bulletin*, 109(6):709–727, 1997.

Sempere, T., Herail, G., Oller, J. and Bonhomme, M. G. Late Oligocene-early Miocene major tectonic crisis and related basins in Bolivia. *Geology*, 18(10):946–949, 1990.

Servant, M., Fontes, J.-C., Rieu, M. and Saliege, J. Holocene arid episodes in southwestern Amazonia. *Comptes Rendus De L Academie Des Sciences Serie II*, 292(18):1295 – 1297, 1981.

Servant, M. and Servant-Vildary, S. Holocene precipitation and atmospheric changes inferred from river paleowetlands in the Bolivian Andes. *Palaeogeography, Palaeoclimatology, Palaeoecology*, 194:187–206, 2003.

Smolders, A., Guerrero Hiza, M., Van der Velde, G. and Roelofs, J. Dynamics of discharge, Sediment transport, heavy metal pollution and Sabalo (Prochilodus Lineatus) Catches in the Lower Pilcomayo River (Bolivia). *River Research and Applications*, 18:415–427, 2002.

Stock, G. M., Frankel, K., Ehlers, T. A., Schaller, M., Briggs, S. and Finkel, R. Spatial and temporal variations in erosion from multiple geochronometers: Wasatch Mountains, Utah, USA. *GSA Lithosphere*, 1:34–40, doi:10.1130/L15.1, 2009.

Stone, J. O. Air pressure and cosmogenic isotope production. *Journal of Geophysical Research*, 105(B10):23,753–23,759, 2000.

Summerfield, M. A. and Hulton, N. J. Natural controls of fluvial denudation rates in major world drainage basins. *Journal of Geophysical Research*, 99(B7):13,871–13,883, 1994.

Uba, C., Kley, J., Strecker, M. R. and Schmitt, A. K. Unsteady evolution of the Bolivian Subandean thrust belt: The role of enhanced erosion and clastic wedge progradation. *Earth and Planetary Science Letter*, 281:134–146, 2009.

von Blanckenburg, F. The control mechanisms of erosion and weathering at basin scale from cosmogenic nuclides in river sediment. *Earth and Planetary Science Letters*, 237(3-4):462–479, 2005.

von Blanckenburg, F., Belshaw, N. S. and O'Nions, R. K. Separation of (super 9) Be and cosmogenic (super 10) Be from environmental materials and SIMS isotope dilution analysis. *Chemical Geology*, 129(1-2):93–99, 1996.

Vuille, M. Atmospheric circulation over the Bolivian Altiplano during dry and wet periods and extreme phases of the Southern Oscillation. *International Journal of Climatology*, 19:1579–1600, 1999.

Wilkinson, B. H. and McElroy, B. J. The impact of humans on continental erosion and sedimentation. *Geological Society of America Bulletin*, 119(1-2):140 – 156, 2007.

Willett, S. Orogeny and orography; the effects of erosion on the structure of mountain belts. *Journal of Geophysical Research*, 104(B12):28957–28982, 1999.

Wittmann, H. and von Blanckenburg, F. Cosmogenic nuclide budgeting of floodplain sediment transfer. *Geomorphology*, 109:246–256, 2009.

Wittmann, H., Von Blanckenburg, F., Guyot, J. L., L, M. and Kubik, P. W. From source to sink: Preserving the cosmogenic 10Be-derived denduation rate signal of the Bolivian Andes in sediment of the Beni and marmore foreland basins. *Earth and Planetary Science Letter*, 288:463 – 474, 2009.

Yanites, B., Tucker, G. E. and Anderson, R. S. Numerical and analytical models of cosmogenic radionuclide dynamics in landslide-dominated drainage basins. *Journal of Geophysical Research*, 114(F01007):doi:10.1029/2008JF001088, 2009.

CHAPTER VI

Summary and conclusions

The principal goals of this dissertation are (1) to quantify changes in precipitation $\delta^{18}O$ associated with South American climate change to evaluate whether regional climate change rather than surface uplift may have caused substantial changes in the stable isotope record; and (2) to understand the role of climate variability in influencing denudation rates. This section summarizes the major results of each dissertation chapter, which in turn provide answers to the motivating questions posed in chapter 1. Finally this chapter highlights the general implications for interpretations of paleoclimate and paleoelevation reconstructions and our understanding of the complex interactions between tectonics, climate, and denudation.

6.1 Result summary

Chapter 2: This chapter quantifies modern variability in the isotopic composition of precipitation $\delta^{18}O_p$ along the Andes and evaluates the significance of individual factors/processes controlling the variability. Model results show: (1) Simulated annual amount-weighted mean $\delta^{18}O_p$ is highly variable along the Andes. The climatological mean $\delta^{18}O_p$ is -5‰ in the northern Andes, up to -13‰ in the northern central Andes, -6‰ in the southern central Andes, and -9‰ in the southern Andes.

(2) Annual isotopic lapse rates on the windward side of the Andes vary between 1.49 and -0.04‰ km^{-1} (northern Andes), -2.46 and -0.05‰ km^{-1} (northern central Andes), -1.39 and -0.42 ‰ km^{-1} (southern central Andes) and -3.16 and -2.46 ‰ km^{-1} (southern Andes). (3) The isotopic composition in the Andes is influenced by multiple factors, including Pacific sea-surface temperatures (northern Andes), precipitation amount, moisture source and vapor trajectory (northern central Andes), wind pattern (southern central Andes), and temperature (southern Andes). Our results emphasize the importance of water vapor source, path, and availability on the $\delta^{18}O_p$ composition across the Andean Plateau and provide constrains for interpreting Andean $\delta^{18}O$ proxy records. In addition, our results emphasize the difficulty in using observed modern climate conditions and isotopic lapse rates to interpret past changes in $\delta^{18}O$ with altitude, because modern conditions change dramatically on spatial and temporal scales and short-term observations in one region may not be representative of mean climate conditions in other regions.

Chapter 3: This chapter presents results from a regional climate modeling study evaluating the influence of the Andes on regional climate over South America. Key results include: (1) The Andes have a significant impact on South American climate by blocking westerly flow from the South Pacific when the Andes reach more than 50% of their modern height. (2) The Andes are critical to the development of the South American low-level jet that draws in moisture from the Amazon Basin and provides the latent energy required to drive convection and precipitation along the Andean front. (3) Uplift of the Andes causes a significant increase in precipitation along the eastern flank of the Andes, more arid conditions along the western flank, and a small decrease in precipitation over the Amazon Basin. (4) South American

atmospheric dynamics similar to modern are established once the Andes reach more than 50% of their modern height and amplify as the Andes rise to their present -day elevation. Understanding the role of the Andes in modulating regional atmospheric conditions has important implications for estimating paleoclimate and paleoelevation histories. Combined with previous studies that show climate shifts along the eastern flank from arid to humid conditions and climate shifts along the western flank from semiarid to hyperarid conditions during the middle to upper Miocene, our results suggest minimum central Andean paleoelevations of >2 km prior to ∼12 Ma.

Chapter 4: This chapter highlights the behavior of $\delta^{18}O_p$ under past topographic and climate conditions and re-evaluates paleoelevation reconstructions based on $\delta^{18}O$ and Δ_{47} clumbed isotopes in late Miocene carbonates. Model results indicate: (1) Simulated changes in $\delta^{18}O_p$ are not systematic with Andean surface uplift, but are instead a function of orographic threshold conditions that abruptly change regional climate. (2) Simulated isotopic compositions of less than -10‰ are generally consistent with elevations >3000 m. (3) A ≥5‰ decrease in $\delta^{18}O_p$ with increasing Andean elevations from 75 to 100% of modern is associated with changes in the low-level atmospheric circulation and precipitation. (4) Isotopic lapse rates change with Andean surface uplift. These findings suggest that the the 3-4‰ shift in $\delta^{18}O$ in Miocene carbonates reflects changes in regional climate associated with relatively minor uplift. The isotopic signal in the ancient carbonate nodules is consistent with Andean paleoelevations of at least ∼3000 m at ∼10 Ma.

Chapter 5: This chapter presents new cosmogenic ^{10}Be and ^{26}Al data to quantify millennial-scale, catchment-averaged denudation rates from the central Andes

and their sensitivity to variations in climate and morphology. The main results from this study are as follows: (1) Cosmogenic radionuclide (CRN) derived denudation rates vary by two orders of magnitude from 0.04 to 1.93 mm yr^{-1} with apparent ages between 0.4 and 20 kyr. (2) Contrary to expectations, CRN derived denudation rates do not reflect present-day latitudinal variations in precipitation. In addition, no statistical correlation exists between CRN derived denudation rates and morphological parameters such as relief or slope. (3) Comparison to ∼130 previously published denudation rates calculated over long (>10^6 yrs), medium ($10^2$$10^4$ yrs), and short timescales (10^1 yrs) indicate Holocene variations in denudation rates that increase significantly over the last ∼5 ka. Denudation rates are characterized by large spatial and temporal variations across the central Andes. The large spatial variability in CRN denudation is most likely due to local variations in tectonics (e.g. faulting), while temporal differences in denudation magnitudes were possibly caused by changes in climate over the integrated time interval with CRN derived denudation rates inheriting a past climate signal.

6.2 Responses to motivating questions

Below are brief answers to the motivating questions posed in chapter 1.

(1) What determines the modern isotopic composition of meteoric water along the Andes?

Overall, the stable isotopic composition of meteoric water ($\delta^{18}O_p$) is determined by the isotopic concentration of the source vapor, isotopic dilution/enrichment through mixing with other air masses, and isotopic fractionation through mass-dependent

processes that act upon the vapor. However, the dominating processes that control modern $\delta^{18}O_p$ vary along the Andes. In the northern Andes, the main factor influencing interannual variability in $\delta^{18}O^p$ is the amount effect with Pacific sea-surface temperatures mainly controlling variations in precipitation. In the northern central Andes, $\delta^{18}O_p$ correlates with precipitation amount, which is related to the position of the Bolivian High and moisture source. In the southern central Andes, $\delta^{18}O_p$ variability is mainly influenced by rainout linked to the strength of zonal winds and vertical ascent on the Andean flanks. In the southern Andes $\delta^{18}O_p$ is mainly influenced by temperature, while the amount effect is negligible due to the location of the southern Andes in the mid-latitude Westerlies and the lack of large convective storms.

(2) What is the effect of Andean surface uplift on regional climate and the processes that control the isotopic composition of precipitation?

Surface uplift of the Andes influences precipitation amount, water vapor source, moisture transport, and dominant low-level wind pattern. The changes in the climatic conditions in response to surface uplift affect isotopic source and amount effects. Andean surface uplift from 250 m to modern elevations effectively blocks westerly flow from the Pacific Ocean and causes a reversal of dominant wind directions in the central Andes from (south-) west to (north-) east. When the Andes reach at least half of their modern height the primary source of Andean precipitation becomes associated with Atlantic moisture recycled via the Amazon Basin. The initiation and strengthening of the South American low-level jet, associated with an increase in Andean elevations, intensifies convergence, orographic lifting, and latent heat release, which fuels convection and convective condensation. Precipitation increases from $\sim$2-4 mm day^{-1} to $>$15 mm day^{-1} along the eastern Andean flank. Greater precipi-

tation results in stronger isotopic fractionation through Rayleigh distillation over the high Andes which causes strong depletion in the isotopic composition of precipitation. However, the climatic and isotopic response to surface uplift is not systematic with elevation gain. Precipitation along the eastern flank increases abruptly when the Andes attain a threshold elevation of ∼75 which leads to a dramatic decrease of $\delta^{18}O_p$ of >5‰ over the Andean Plateau when the Andes are uplifted from ∼3000 to 4000 m.

(3) How does climate change impact the interpretation of Andean paleoelevations?

The documented changes in South American climate and in the isotopic composition of precipitation suggest that the growth of the Andes was not rapid and recent (Fig. 6.1). The onset of hyperaridity along the west coast of South America prior to 12-15 Ma has been related to the rain shadow effect of the Andes. To block the low-level zonal flow from and to the Pacific Ocean and to reduce the moisture along the western flank, Andean elevations need to attain at least 50% of their modern height, thus, suggesting minimum Andean elevations of at least 2000 m prior to 12 Ma. A 5‰ decrease in $\delta^{18}O$ associated with chances in the low-level atmospheric circulation and precipitation in response to Andean surface uplift from 75 to 100% of modern elevations, could account for the entire change in the isotopic composition of carbonate nodules between 10 and 6 Ma. That is in agreement with low $\delta^{18}O$ compositions (generally less than -10‰) in 11-10 Ma old carbonate nodules that are consistent with modern $\delta^{18}O_p$ compositions at elevations above 3000 m. The integration of simulated and observed isotopic compositions in precipitation and regional climate change suggests that the $\delta^{18}O$ depletion in late Miocene carbonates mainly reflects the intensification of precipitation associated with relatively minor surface

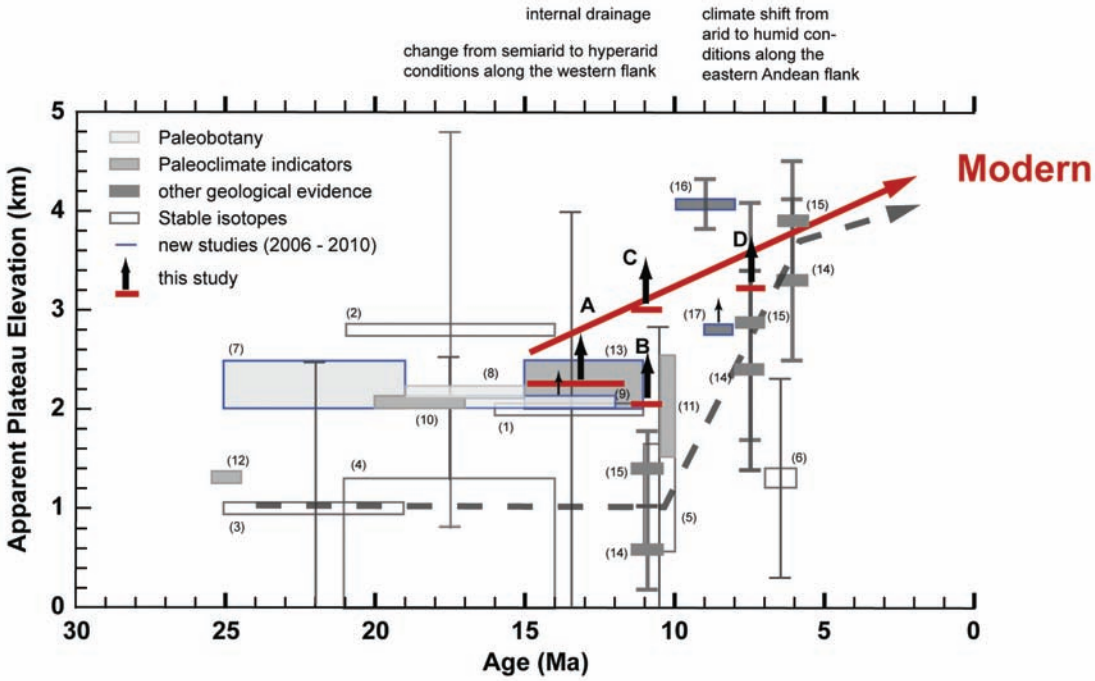

Model results - climate corrected data

A RegCM results indicate that at least 50% (>2 km) of Andean elevations are necessary to block westerly flow and to create a rainshadow as proposed by (8, 9)

B GENESIS simulations indicate that changes in the d^{18}O composition of meteoric water with Andean surfac uplift from 50 to 100% modern elevations can account for the entire d^{18}O shift in ancient carbonate nodules between 10 and 6 Ma -> suggests elevations above 2 km

C REMOiso results suggest that d^{18}O compositions of > -10‰ in ancient carbonate nodules (11.5 - 10.3 Ma) mainly reflect fractionation processes at elevations above 3000 m

C REMOiso simulations demonstrate that d^{18}O decreases by >5‰ with Andean surface uplift from 75% to 100%, a depletion that accounts for the entire change in the isotpic composition of carbonate nodules between 10 and 6 Ma

D same as C, for carbonates dated between 10.3 and 6.8 Ma

Figure 6.1: Climate corrected paleoelevation history of the central Andes. Apparent Plateau elevation (km) is plotted against age (Ma). Gray boxes represent paleoelevation estimations from previous studies; dashed, dark gray line highlights the previous interpretation of fast and recent AP uplift. Horizontal red lines and black arrows (A-D) represent climate corrected data from this thesis. Bold red arrow shows the re-interpreted surface uplift history of the central Andes since 15 Ma. Previous studies of AP uplift: Paleobotany: (1) Singewald and Berry (1922), (2) Berry (1939), (3) Munoz and Charrier (1996), (4) Gregory-Wodzicki et al. (1998), (5) Gregory-Wodzicki et al. (1998), (6) Graham et al. (2001), (7) Picard et al. (2008); Paleoclimate indicators: (8) Alpers and Brimhall (1988), (9) Rech et al. (2006); other geological evidence: (10) Sebrier et al. (1988), (11) Gubbels et al. (1993), (12) Lamb and Davis (2003), (13) Schlunegger et al. (2010); Stable Isotopes: (14) Ghosh et al. (2006); Quade et al. (2007), (15) Garzione et al. (2006), (16) Bershaw et al. (2010), (17) Mulch et al. (2010)

uplift; and that the Andes attained an elevation of ∼3000 m at ∼10 Ma.

6.3 Evaluation of Hypotheses and Future work

Much of the work presented here focuses on the controversy about the timing and rate of Andean Plateau uplift and its influence on regional climate and $\delta^{18}O_p$. Results suggest that the apparent rapid, recent rise of the Andean Plateau in the late Miocene based on stable isotope and paleobotanical records are artifacts of changes in South American atmospheric circulation and climate during the Cenozoic (Ehlers and Poulsen, 2009). Significant modifications in moisture sources, transport, and availability occur when the Andes attain a threshold elevation of 2.5 to 3 km. The change in prevailing wind directions and vapor source strongly influences precipitation along the Andes and substantially contribute to changes in $\delta^{18}O_p$ previously interpreted as reflections of surface uplift. The thesis proves that major changes in the $\delta^{18}O$ in ancient carbonate nodules are most likely related to changes in South American climate associated with relatively minor surface uplift. In addition, this project shows that $\delta^{18}O_p$ is influenced by processes not accounted for in traditional paleoaltimetry estimates and that paleoclimate modeling studies are necessary to provide additional constrains on the interpretation of soil carbonate $\delta^{18}O$ records and to redefine the uplift history of the Andes.

The approach to quantify past changes in climate in response to Andean surface uplift involves the use of limited-domain general circulation models (RCMs). In theory, RCMs can be used to simulate and investigate past changes in climate and their influence on stable isotopes. In practice, despite the higher horizontal and vertical resolution in comparison to global general circulation models, RCMs still have

deficiencies that might bias their simulation. Over the Andes, these deficiencies are mostly related to the physical parameterizations (particularly of convective and land-surface processes) and local representation of mountainous regions. However, results shows that RCMs simulate precipitation and stable isotopes that are in good agreement with the sparse available observations in South America and the Andean region (e.g., Garcia et al., 1998; Aravena et al., 1999; Gonfiantini et al., 2001; Stern and Blisniuk, 2002). The models are able to (a) simulate interannual climate variations over South America and replicate observed meteorological - $\delta^{18}O_p$ relationships from the Andes (chapter 2 and 3), and (b) provide specific predictions of past changes in climate and stable isotopes in response to different Andean topographies that can be directly compared to carbonate $\delta^{18}O_p$ in paleosols and used for paleoclimate studies (chapter 3 and 4).

The presented work also addresses the hypothesis that climate variability is reflected in the spatial and temporal variability of denudation rates along the Andes. Short-term (10^1-10^2 yrs) denudation rates indicate a disparity with $\sim$3 times higher mean denudation rates in more humid regions compared to drier regions, while medium-term (10^2-10^4 yrs) denudation rates do not reflect the modern precipitation pattern. On millenial timescales climate changes significantly and long-term denudation rates may reflect climatic conditions integrated over numerous cycles. Along the central Andes, denudation rates show a three-fold increase over the last several thousand years that is most likely related to an increase in precipitation since 4.5 ka. Although numerical model results suggest that climate shifts towards more humid conditions and/or towards more variable conditions in the central Andes may have had a substantial influence on denudation rates, it remains difficult to constrain. Overall, the topography reflects tectonics and the overprint of multiple

climate driven processes and related effects in changes of erosional efficiency. Unfortunately, the importance of tectonics versus climate forcing at different length and time scales remains elusive.

Finally, this thesis shows the importance to identify and understand the various interactions between tectonics, climate, and denudation, since the forces acting on an evolving landscape are neither spatially nor temporally consistent. Although we begin to understand some of these processes, numerous open questions remain. For example, it is still not very well known what the necessary time scales are to generate topographic changes, which kind of denudation processes are the most efficient, and most importantly, which climatic and topographic thresholds exists to significantly alter a tectonically active system. Higher resolution ($\sim$20 km) general circulation models simulating climatic changes on finer topographic scales would allow refining threshold elevations for the initiation of climate pattern. For example, Andean heights could be specified at 50, 60, 70, 80, 90, and 100% of modern elevations, or experiments can be conducted in which the lateral extent of the Andes increases stepwise at $\sim$100 km increments. Dynamic land-surface models fully coupled with high resolution ($<$5 km) climate models could also help to disentangle the relationships between tectonic activity, climate patterns, and surface processes. In addition, more observations are needed to better understand the effects and causes of climate variability and surface processes. For example, on short-timescales better climate records and high precision dating of landslides and denudation would allow to detect direct relationships between sustained periods of precipitation and mass movement. On long timescales, more paleoclimate observations and simulations are necessary to link sustained climate conditions to observed changes in surface processes (e.g. river incision).

Bibliography

Alpers, C. N. and Brimhall, G. H. Middle Miocene climate change in the Atacama Desert, northern Chile: Evidence from supergene mineralization at La Escondida. *Geological Society of America Bulletin*, 100:1640 – 1656, 1988.

Aravena, R., Suzuki, O., Pena, H., Pollastri, A., Fuenzalida, H. and Grilli, A. Isotopic composition and origin of the precipitation in Northern Chile. *Applied Geochemistry*, 14:411–422, 1999.

Berry, E. W. The fossil flora of Potosi, Bolivia. *Johns Hopkins University Studies in Geology*, 13:1–67, 1939.

Bershaw, J., Garzione, C. N., Higgins, P., MacFadden, B., Anaya, F. and Alvarenga, H. Spatial-temporal changes in Andean plateau climate and elevation from stable isotopes of mammal teeth. *Earth and Planetary Science Letter*, 289:530 – 538, 2010.

Ehlers, T. and Poulsen, C. J. Influence of Andean uplift on climate and paleoaltimetry estimates. *Earth and Planetary Science Letter*, 281:238–248, 2009.

Garcia, M., Villalba, F., Araguas Araguas, L. and Rozanski, K. The role of atmospheric circulation patterns in controlling the regional distribution of stable isotope contents in precipitation. *Isotope techniques in the study of environmental change*, IAEA-SM-349/7: Vienna, International Atomic Energy agency:127–140, 1998.

Garzione, C. N., Molnar, P., Libarkin, J. and MacFadden, B. Rapid late Miocene rise of the Bolivian Altiplano: Evidence for removal of mantle lithosphere. *Earth and Planetary Science Letters*, 241:543–556, 2006.

Ghosh, P., Garzione, C. and Eiler, J. Rapid uplift of the Altiplano revealed through 13C-18O bonds in paleosol carbonates. *Science*, 311:511 – 515, 2006.

Gonfiantini, R., Roche, M.-A., Olivry, J.-C., Fontes, J.-C. and Zuppi, G. M. The altitude effect on the isotopic composition of tropical rains. *Chemical Geology*, 181:147 – 167, 2001.

Graham, A., Gregory-Wodzicki, K. M. and Wright, K. L. A Mio-Pliocene palynoflora from the Eastern Cordillera, Bolivia: implications for the uplift history of the central Andes. *American Journal of Botany*, 88(9):1545–1557, 2001.

Gregory-Wodzicki, K. M., McIntosh, W. C. and Velasquez, K. Climatic and tectonic implications of the late Miocene Jakokkota Flora, Bolivian Altiplano. *Journal of South American Earth Sciences*, 11(6):533–560, 1998.

Gubbels, T. L., Isacks, B. L. and Farrar, E. High-level surfaces, plateau uplift, and foreland development, Bolivian central Andes. *Geology*, 21(8):695–698, 1993.

Lamb, S. and Davis, P. Cenozoic climate change as a possible cause for the rise of the Andes. *Nature*, 425:792–797, 2003.

Mulch, A., Uba, C., Strecker, M. R., Schoenberg, R. and Chamberlain, C. P. Late Miocene climate variability and surface elevation in the central Andes. *Earth and Planetary Science Letter*, 290:173 – 182, 2010.

Munoz, N. and Charrier, R. Uplift of the western border of the Altiplano on a west-vergent thrust system, Northern Chile. *Journal of South American Earth Sciences*, 9(3-4):171–181, 1996.

Picard, D., Sempere, T. and Plantard. Direction and timing of uplift propagation in the Pervian Andes dedcued from molecular phylogenetics of highland biotaxa. *Earth and Planetary Science Letter*, 271:326 – 336, 2008.

Quade, J., Garzione, C. and Eiler, J. Paleoelevation reconstructions using pedogenic carbonates. *Reviews in Mineralogy and Geochemistry*, 66:53–87, 2007.

Rech, J. A., Currie, B. S., Michalski, G. and Cowan, A. M. Neogene climate change and uplift in the Atacama Desert, Chile. *Geology*, 34(9):761–764, 2006.

Schlunegger, F., Kober, F., Zeilinger, G. and von Rotz, R. Sedimentology-based reconstructions of paleoclimate changes in the Central Andes in response to the uplift of the Andes, Arica region between 19 and 21?S latitude, northern Chile. *International Journal of Earth Sciences*, pages doi:10.1007/s00531–010–0572–8, 2010.

Sebrier, M., Lavenu, A., Fornari, M., Soulas, J. P. and Anonymous. Tectonics and uplift in Central Andes (Peru, Bolivia and northern Chile) from Eocene to present. In *Seminaire; Geodynamique des Andes centrales. Seminar on Geodynamics of the Central Andes*, volume 3, pages 85–106. Office de la Recherche Scientifique et Technique Outre-Mer (ORSTOM), Bondy, 1988.

Singewald, J. T. and Berry, E. W. The geology of the Corocoro copper district of Bolivia. *Johns Hopkins University Studies in Geology*, 1:1–117, 1922.

Stern, L. A. and Blisniuk, P. M. Stable isotope composition of precipitation across the southern Patagonian Andes. *Journal of Geophysical Research*, 107(D23)(4667):doi:10.1029/2002JD002509, 2002.